




## ARTICLE

# The Rab7 effector WDR91 promotes autophagy-lysosome degradation in neurons by regulating lysosome fusion

Ruxiao Xing<sup>1\*</sup>, Hejiang Zhou<sup>2\*</sup>, Youli Jian<sup>1</sup>, Lingling Li<sup>1</sup>, Min Wang<sup>1</sup>, Nan Liu<sup>2</sup>, Qiuyuan Yin<sup>2</sup>, Ziqi Liang<sup>1</sup>, Weixiang Guo<sup>1</sup>, and Chonglin Yang<sup>2</sup>

The effectors of the Rab7 small GTPase play multiple roles in Rab7-dependent endosome-lysosome and autophagy-lysosome pathways. However, it is largely unknown how distinct Rab7 effectors coordinate to maintain the homeostasis of late endosomes and lysosomes to ensure appropriate endolysosomal and autolysosomal degradation. Here we report that WDR91, a Rab7 effector required for early-to-late endosome conversion, is essential for lysosome function and homeostasis. Mice lacking *Wdr91* specifically in the central nervous system exhibited behavioral defects and marked neuronal loss in the cerebral and cerebellar cortices. At the cellular level, WDR91 deficiency causes PtdIns3P-independent enlargement and dysfunction of lysosomes, leading to accumulation of autophagic cargoes in mouse neurons. WDR91 competes with the VPS41 subunit of the HOPS complex, another Rab7 effector, for binding to Rab7, thereby facilitating Rab7-dependent lysosome fusion in a controlled manner. WDR91 thus maintains an appropriate level of lysosome fusion to guard the normal function and survival of neurons.

## Introduction

Neuronal development and survival require the normal function of lysosome-centered endosome-lysosome and autophagy-lysosome pathways, which enable accurate regulation of developmental signals and timely removal of aggregated proteins and damaged organelles (Ballabio and Bonifacino, 2020; Cecconi and Levine, 2008; Levine and Klionsky, 2004; Yap and Winckler, 2012). Dysfunction of lysosomes is a causative factor in the pathogenesis of neurological disorders. For example, abnormally enlarged and dysfunctional lysosomes are found in familial Kufor-Rakeb syndrome and Charcot-Marie-Tooth disease 4J, which are caused by mutations in the lysosomal P5-type ATPase ATP13A2 and the phosphoinositide phosphatase FIG4, respectively (Dehay et al., 2012; Lenk et al., 2011; Ramirez et al., 2006). Notably, dysfunction of lysosomes causes failure to degrade autophagic substrates such as pathogenic protein aggregates, leading to neuronal death in neurodegenerative diseases (Farfel-Becker et al., 2019; Orr and Oddo, 2013; Pan et al., 2008).

The homeostatic maintenance of lysosomes involves multiple mechanisms, including lysosome biogenesis, reformation, dynamic fusion, and division (Durchfort et al., 2012; Rocznik-Ferguson et al., 2012; Yu et al., 2010). Lysosomal fusion with

late endosomes and autophagosomes is critical for delivery and degradation of endocytic and autophagic cargoes. The fusion of late endosomes/lysosomes initiates with membrane tethering that is controlled by Rab7 (Ypt7 in yeast), a GTPase that defines the identity of the late endosomal/lysosomal compartments and is required for the sorting of acidic hydrolases and formation of functional lysosomes (Balderhaar et al., 2010; Langemeyer et al., 2018). As an effector of Rab7/Ypt7, the homotypic fusion and protein sorting (HOPS) complex mediates membrane tethering and assembles the SNARE complex to fulfill fusion (Balderhaar and Ungermann, 2013; Krämer and Ungermann, 2011; Lürick et al., 2018). HOPS is a multi-subunit complex consisting of VPS11, 16, 18, 33, 39, and 41. Yeast HOPS adopts a seahorse shape, with two Ypt7-binding subunits, Vps41 and Vps39, located at the “head” and “tail,” respectively (Bröcker et al., 2012; Chou et al., 2016; Kuhlee et al., 2013). In mammals, it is not clear whether Rab7 directly interacts with VPS41. It has been reported that some effectors of Rab7 interact with HOPS to promote fusion between late endosomes and lysosomes and fusion of late endosomes/lysosomes with autophagosomes. For example, PLEKHM1 (pleckstrin homology domain containing protein

<sup>1</sup>State Key Laboratory of Molecular Developmental Biology, Institute of Genetics and Developmental Biology, Chinese Academy of Sciences, Beijing, China; <sup>2</sup>State Key Laboratory of Conservation and Utilization of Bio-Resources in Yunnan and Center for Life Science, School of Life Sciences, Yunnan University, Kunming, China.

\*R. Xing and H. Zhou contributed equally to this paper; Correspondence to Chonglin Yang: [clyang@ynu.edu.cn](mailto:clyang@ynu.edu.cn); Weixiang Guo: [wxguo@genetics.ac.cn](mailto:wxguo@genetics.ac.cn); Hejiang Zhou: [zhouhejiang@ynu.edu.cn](mailto:zhouhejiang@ynu.edu.cn).

© 2021 Xing et al. This article is distributed under the terms of an Attribution-Noncommercial-Share Alike-No Mirror Sites license for the first six months after the publication date (see <http://www.rupress.org/terms/>). After six months it is available under a Creative Commons License (Attribution-Noncommercial-Share Alike 4.0 International license, as described at <https://creativecommons.org/licenses/by-nc-sa/4.0/>).

family member 1) interacts with Rab7 and VPS41 to promote fusion of late endosomes with lysosomes (McEwan et al., 2015b). PLEKHM1 also interacts with LC3 to facilitate autophagosome-lysosome fusion (McEwan et al., 2015a). The Vici syndrome protein EPG5 acts as a Rab7 effector to determine the fusion specificity of autolysosomes and late endosomes by interacting with SNARE proteins (Wang et al., 2016). In addition, Rab-interacting lysosomal protein, another Rab7 effector, interacts with the VPS41 subunit of HOPS, promoting HOPS recruitment to late endosomes (Lin et al., 2014). Rab7 has multiple effectors, but it remains largely unknown how these effectors coordinate to regulate the fusion of late endosomes/lysosomes and fusion of autophagosomes with late endosomes/lysosomes.

The WD40 repeat-containing protein WDR91 was recently identified as a Rab7 effector (Liu et al., 2017). WDR91 forms a complex with WDR81, another WD40-repeat protein, and is recruited to endosomes by active GTP-bound Rab7. Once on the endosomes, the WDR91-WDR81 complex further interacts with the Beclin 1 subunit of the phosphatidylinositol 3-kinase (PI3K) complex, thus inhibiting Rab7-associated PI3K activity. This facilitates early-to-late endosome conversion in the endosome-lysosome pathway. Loss of either WDR91 or WDR81 leads to formation of giant intermediate endosomes (Liu et al., 2016; Liu et al., 2017). Notably, brain-specific depletion of *Wdr91* in mice causes defective dendritic arborization and reduced brain size, with accumulation of apoptotic cells (Liu et al., 2017). Similarly, knockout of *Wdr81* in the brain leads to early death of mice, which exhibit neuronal accumulation of autophagic substrates, altered hippocampal neurogenesis, and impaired hippocampus-dependent learning (Wang et al., 2021). Although the WDR91-WDR81 complex serves as a Rab7 effector, it remains unknown whether one or both proteins play an important role in regulating the fusion of late endosomes/lysosomes.

In this study, we investigate the mechanisms by which WDR91 regulates lysosome fusion and hence lysosomal homeostasis. We show that mice lacking *Wdr91* specifically in the central nervous system display progressive motor and behavioral defects and marked neuronal loss in the cerebral and cerebellar cortices. We reveal that abnormal enlargement of lysosomes accounts for neuronal accumulation of LC3 puncta, p62 aggregates, and ubiquitin-positive inclusions, which contribute to neuronal death in *Wdr91*-deficient mice. Mechanistically, we demonstrate that WDR91 competes with VPS41 for binding to Rab7. Loss of WDR91 increases lysosome fusion, leading to abnormal lysosome enlargement and dysfunction. These findings demonstrate that WDR91 is important for lysosome homeostasis and neuronal autophagy by maintaining an appropriate level of lysosome fusions.

## Results

### Loss of WDR91 leads to neuronal degeneration

Brain-specific knockout of *Wdr91* in mice (*Wdr91<sup>fl/fl</sup>; Nestin-Cre, Wdr91* cKO) was found to cause progressive growth retardation, smaller brain size, and postnatal death at ~4 wk of age (Liu et al., 2017). To further understand the requirement for WDR91 in neuronal development and function, we evaluated the behavior of *Wdr91* cKO mice. Compared with WT, *Wdr91* cKO mice at

postnatal day 21 (P21) showed an ataxic walking pattern in footprint assays (Fig. 1 A) and impaired motor coordination in rotarod assays (Fig. 1 B). In tail-suspension assays, *Wdr91* cKO mice displayed limb-clasping reflexes, while WT mice extended the limbs (Fig. 1 C). These behavioral abnormalities, which are often seen in mice with neurodegeneration, suggest that brain-specific deletion of *Wdr91* likely causes neurological defects.

We next performed hematoxylin and eosin (H&E) staining to examine the brain defects in *Wdr91* cKO mice at P21. The corpus callosum is a bundle of nerve fibers that connects the left and right sides of the brain, thus enabling communication between the two cerebral cortexes. Compared with WT, *Wdr91* cKO mice exhibited severe atrophy of corpus callosum (Fig. 1 D). The abundance of myelin basic protein (MBP) was significantly reduced in *Wdr91* cKO mice (Fig. S1 A). Specific deletion of *Wdr91* in oligodendrocyte progenitors, however, did not obviously affect the expression of MBP (Fig. S1 A), suggesting that the atrophy of corpus callosum was probably not due to impaired oligodendrocyte differentiation in *Wdr91* cKO mice. Interestingly, a number of eosinophilic spheroids were observed in the corpus callosum of *Wdr91* cKO mice (Fig. 1 E), indicating that the cortical projection neurons were swollen. In total, ~30% of *Wdr91<sup>-/-</sup>* neurons were found to be swollen and enclosed by thinner myelin than WT under transmission electron microscopy (TEM; Fig. 1 F). Remarkably, these swollen axons accumulated a number of enlarged lysosomal structures (Fig. 1 G). Importantly, we detected a highly significant increase in the number of cells positive for activated Caspase 3 (AC3) cells (Fig. 1 H) and the numbers of GFAP-positive astrocytes and Iba1-positive microglial cells in the cerebral cortex of *Wdr91* cKO mice compared with WT (Fig. S1, B and C). Moreover, *Wdr91* cKO mice had a significantly increased number of AC3-positive cells (Fig. S1 D) and a greatly reduced number of Calbindin-positive Purkinje cells (which are involved in physical movement) in the cerebellum (Fig. 1 I). Taken together, these results suggest that loss of *Wdr91* in the brain leads to neurodegeneration.

### Lysosomes are abnormally enlarged and dysfunctional in *Wdr91<sup>-/-</sup>* neurons

Neuron survival and development largely rely on appropriate lysosome-dependent autophagy (Cai et al., 2010; Winckler et al., 2018). Because the swollen neurons in the brain of *Wdr91* cKO mice accumulated abnormally enlarged lysosomal structures, we investigated how WDR91 plays a role in lysosome homeostasis and autophagy. Similar to WDR91 knockout (KO-91) HeLa cells (Liu et al., 2016; Liu et al., 2017), the cortical neurons from *Wdr91* cKO mice accumulated abnormally enlarged LAMP1-positive structures, which were mainly seen in the soma (Fig. 2 A). In addition, the LAMP1-enriched large compartments had very limited costaining with EEA1. Further costaining of cathepsin D (CTSD) with LAMP1 revealed no discernible difference between *Wdr91<sup>-/-</sup>* neurons and WT (Fig. 2 B), and the CTSD/LAMP1 costaining ratio was in agreement with previous reports (Cheng et al., 2018; Yap et al., 2018). These findings suggest that these enlarged LAMP1-positive vesicles are late endosomes/lysosomes. Using LysoSensor Blue DND-160, which produces blue fluorescence in a neutral environment but shifts to yellow

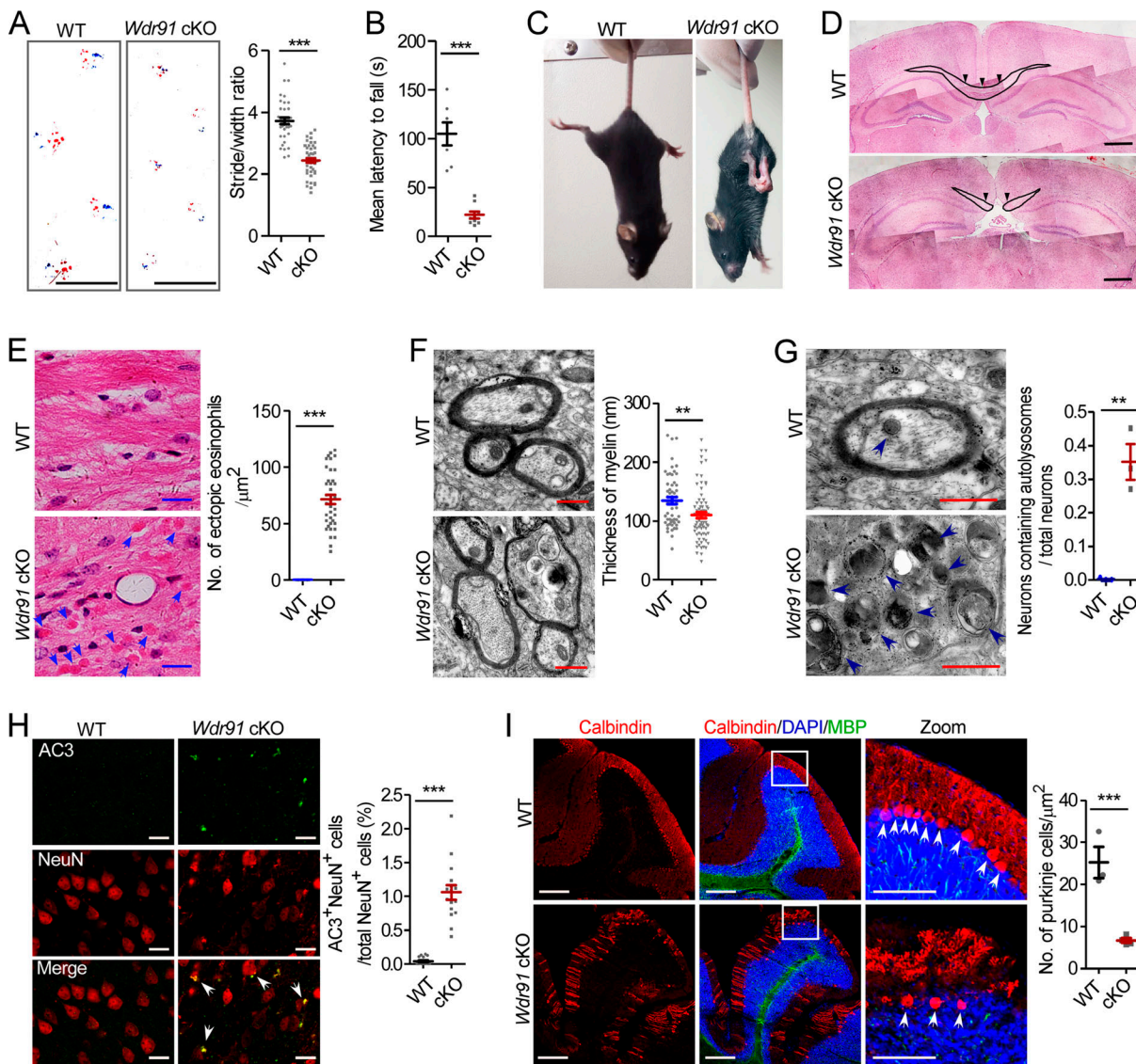


**Figure 1. Loss of WDR91 leads to neuron degeneration.** (A) Representative footprint images of WT and *Wdr91* cKO mice at P21. Scale bars, 1 cm. The ratio of stride length to width from WT ( $n = 7$ ) and *Wdr91* cKO ( $n = 8$ ) mice is shown on the right. Five to six steps were analyzed for each animal. (B) Duration of the rotating rod of WT ( $n = 7$ ) and *Wdr91* cKO ( $n = 9$ ) mice at P21. (C) Representative images of WT and *Wdr91* cKO mice at P21 in tail-suspension assays. (D) H&E staining of brain sections of WT and *Wdr91* cKO mice at P21. The corpus callosum is outlined with black lines. Scale bars, 1,000  $\mu\text{m}$ . (E) H&E staining of the corpus callosum in coronal sections of WT and *Wdr91* cKO mice at P21. Blue arrows indicate eosinophilic spheroids. Scale bars, 20  $\mu\text{m}$ . Quantification of ectopic eosinophilic spheroids (39 sections from three mice for each genotype) is shown on the right. (F) Representative TEM images of myelin in the brain of WT and *Wdr91* cKO mice at P21. Scale bars, 0.5  $\mu\text{m}$ . Quantification of myelin thickness (15 sections from three mice for each genotype) is shown on the right. (G) Representative TEM images of autolysosomes (blue arrowheads) in the brain of WT and *Wdr91* cKO mice at P21. Scale bars, 0.5  $\mu\text{m}$ . Quantification of the proportion of neurons containing autolysosomes (200 sections from three mice for each genotype) is shown on the right. (H) Representative images (left) and quantification (right) of AC3<sup>+</sup> (green) staining of NeuN<sup>+</sup> (red) neurons in coronal sections of cerebral cortex of WT and *Wdr91* cKO mice at P21. AC3<sup>+</sup> cells are indicated with arrows. Scale bars, 50  $\mu\text{m}$ . 24 sections from three mice for each genotype were scored. (I) Representative images (left) and quantification (right) of staining of Calbindin (red) and MBP (green) in coronal sections of cerebral cortex of WT and *Wdr91* cKO mice at P21. Scale bars, 200  $\mu\text{m}$ . Boxed regions in the middle images are magnified and shown in the right images. Calbindin staining of Purkinje cells is indicated with arrows. Nuclei are stained with DAPI (blue). Scale bars, 100  $\mu\text{m}$ . 30 sections from three mice for each genotype were analyzed. For all quantifications, error bars represent SEM. Data were from three independent experiments. \*\*,  $P < 0.01$ ; \*\*\*,  $P < 0.001$ .

fluorescence in more acidic compartments, we found that LAMP1-positive lysosomes produced yellow fluorescence in WT neurons. However, the enlarged lysosomes in *Wdr91*<sup>-/-</sup> neurons showed only weak yellow fluorescence (Fig. 2 C), indicating that the pH in these enlarged lysosomes was elevated. We next examined the proteolytic processing of lysosomal cathepsins B and

D. Compared with WT, *Wdr91* cKO mouse brains accumulated the pro-forms (enzyme precursors) of cathepsins B and D, and the cleaved mature forms were reduced (Fig. 2, D and E). Consistent with this, lysosomes in *Wdr91*<sup>-/-</sup> neurons were not stained by Magic Red and Bodipy-FL-pepstatin A, the dyes that respectively indicate the activities of cathepsins B and D

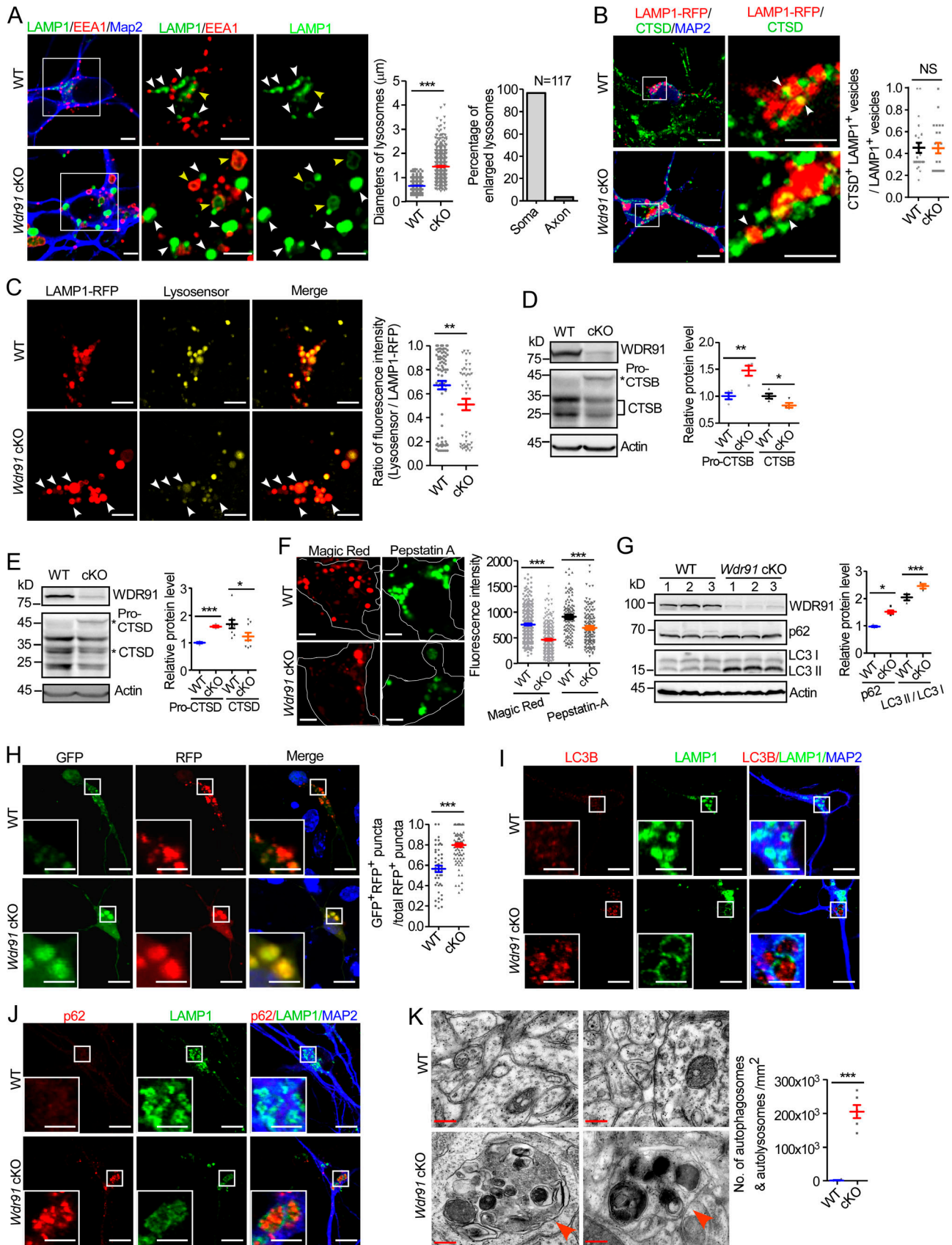


Figure 2. **Loss of WDR91 causes lysosome defects.** (A) Left: Immunostaining of LAMP1 (green), EEA1 (red), and the neuronal marker Map2 (blue) in cultured primary cortex neurons isolated from WT and *Wdr91* cKO mice. Boxed regions are magnified and shown on the right. Organelles with strong LAMP1 staining are

indicated with white arrowheads. EEA1-positive organelles with weak LAMP1 staining are indicated with yellow arrowheads. Scale bars, 5  $\mu\text{m}$ . Middle: Quantification of lysosomal diameters ( $\geq 570$  vesicles from 114 neurons for each genotype). Right: Quantification of enlarged lysosomes in the soma or axon of *Wdr91*<sup>-/-</sup> neurons. 117 enlarged LAMP1-organelles in 29 *Wdr91*<sup>-/-</sup> neurons were analyzed. **(B)** Left: Immunostaining of CTSD (green) and Map2 (blue) in cultured primary cortex neurons expressing LAMP1-RFP. Neurons were isolated from WT and *Wdr91* cKO mice and transfected with the vector expressing LAMP1-RFP. Cells were immunostained and imaged 24 h after transfection. Scale bars, 10  $\mu\text{m}$ . Boxed regions are magnified and shown on the right. White arrowheads indicate organelles that are double positive for LAMP1 and CTSD. Scale bars, 5  $\mu\text{m}$ . The ratio of CTSD- and LAMP1-positive vesicles to total LAMP1-vesicles from  $\geq 22$  cells for each genotype is shown on the right. **(C)** LysoSensor staining in cultured primary cortex neurons (left). Cells were stained and imaged 24 h after transfection of the vector expressing LAMP1-RFP. Arrowheads indicate the enlarged lysosomes with weaker yellow fluorescence. Scale bars, 5  $\mu\text{m}$ . The ratio of fluorescence intensity of LysoSensor to LAMP1-RFP from  $\geq 45$  cells for each genotype is shown on the right. **(D and E)** Immunoblotting analysis of CTSB (D) and CTSD (E) in brain homogenates of WT and *Wdr91* cKO mice. Quantification of protein levels of three mice for each genotype are shown in the right panels. **(F)** Bodipy-Pepstatin A and Magic Red staining in cultured primary cortex neurons (left). Scale bars, 5  $\mu\text{m}$ . White lines mark the border of the cells. Quantification of fluorescence intensity of  $\geq 114$  cells for each group is shown on the right. **(G)** Immunoblotting of LC3 and p62 in brain homogenates of WT and *Wdr91* cKO mice (left). Quantification of protein levels is shown on the right. Three animals of each genotype were analyzed. **(H)** Representative images and quantification of RFP-GFP-LC3 in cultured primary cortex neurons isolated from WT and *Wdr91* cKO mice (left). Cells were imaged 24 h after transfection of the vector expressing RFP-GFP-LC3. Scale bars, 10  $\mu\text{m}$ . Boxed regions are magnified and shown on the bottom left in each image. Scale bars, 5  $\mu\text{m}$ . The ratio of GFP<sup>+</sup>RFP<sup>+</sup> puncta to total RFP<sup>+</sup> puncta in  $\geq 45$  cells is quantified on the right. **(I and J)** Immunostaining of LC3B (red; I) and p62 (red; J) with LAMP1 (green) in cultured primary cortex neurons (stained with Map2 in blue). Scale bars, 10  $\mu\text{m}$ . Boxed regions are magnified and shown on the bottom left in each image. Scale bars, 5  $\mu\text{m}$ . **(K)** Representative TEM images of autophagosomes and autolysosomes (red arrowheads) in brain cortex of WT and *Wdr91* cKO mice (left). Scale bars, 0.2  $\mu\text{m}$ . The number of autophagosomes and autolysosomes is quantified on the right. 200 sections from three mice for each genotype were scored. For all quantifications, data were from three independent experiments. Error bars represent SEM. \*,  $P < 0.05$ ; \*\*,  $P < 0.01$ ; \*\*\*,  $P < 0.001$ .

(Fig. 2 F). Taken together, these results demonstrated that the enlarged lysosomes are dysfunctional in *Wdr91*<sup>-/-</sup> neurons.

Next, we assessed how the dysfunctional lysosomes affected autophagy in the brains of *Wdr91* cKO mice. Significant increases in p62 and LC3-II levels were detected in the brains of *Wdr91* cKO mice (Fig. 2 G). Immunostaining further indicated that p62 and ubiquitin colocalized in foci in *Wdr91* cKO mouse brain (Fig. S2 A). Moreover, *Wdr91* cKO mice accumulated LC3 foci in NeuN<sup>+</sup> neurons in the brain (Fig. S2 B). The accumulation of p62- and ubiquitin-positive inclusions and LC3 puncta might result from defective autophagy or impaired lysosomal degradation. To distinguish between these possibilities, we employed a tandem RFP-GFP-LC3 reporter to pinpoint the defects in the autophagy-lysosome pathway. In autophagosomes, both GFP and RFP signals are detected, whereas in autolysosomes the GFP signal is quenched in the acidic lumen while the RFP fluorescence remains stable. In WT neurons, among all RFP-positive puncta (representing the total number of autophagosomes and autolysosomes), ~60% were also positive for GFP (representing autophagosomes; Fig. 2 H). In *Wdr91*<sup>-/-</sup> neurons, however, GFP- and RFP-positive puncta mostly overlapped, and the sizes were greatly increased (Fig. 2 H), suggesting that the autolysosomes were not functional. In addition, most LC3 puncta and p62 aggregates were found to colocalize with the enlarged LAMP1-positive lysosomes in *Wdr91*<sup>-/-</sup> neurons (Fig. 2, I and J). This suggests that the autophagic cargoes were successfully delivered to lysosomes but failed to be degraded. With TEM, few autophagic structures were observed in WT mouse brain. In contrast, *Wdr91* cKO mice accumulated many densely stained autophagic structures, which are autolysosomes containing undigested substrates (Fig. 2 K). Taken together, these data suggest that WDR91 deficiency leads to enlarged and dysfunctional lysosomes, which impair autophagic cargo degradation and hence the autophagy-lysosome pathway.

### WDR91 deficiency promotes lysosome fusion

We next investigated how lysosomes are abnormally enlarged in the absence of WDR91. First, we tested whether loss of WDR91

affects fusion of lysosomes. Incubation of cells with acetate Ringer's solution (AR) induces lysosome fragmentation and movement to the periphery of the cell, and reculture of the cells in normal medium enables lysosomes to move to the perinuclear region and re-fuse (Heuser, 1989). In KO-91 HeLa cells, AR induced fragmentation of the enlarged lysosomes, although the sizes of these fragmented lysosomes were still larger than those in control cells that were similarly treated (Fig. 3 A). A more detailed time-lapse analysis indicated that AR treatment led to generation and release of LAMP1-positive tubules in both control and KO-91 HeLa cells (Fig. S3). Following removal of AR, lysosomes were restored to their original sizes in both control and KO-91 HeLa cells; however, fusion of large lysosomes with much smaller lysosomes was constantly observed in KO-91 cells, and the lysosome sizes significantly increased over time compared with the control cells (Fig. 3, B and C). In *Wdr91*<sup>-/-</sup> mouse neurons, AR also induced fragmentation of the enlarged lysosomes, and their re-fusion rate as well as their sizes were significantly enhanced following removal of AR (Fig. 3, D and E). These results suggest that loss of WDR91 increased the ability of lysosomes to fuse. To corroborate this conclusion, we treated HeLa cells with vacuolin-1, which is known to induce lysosomal enlargement (Cerny et al., 2004), and monitored lysosomal change over time. In KO-91 HeLa cells, vacuolin-1 caused much faster lysosome enlargement than in the control cells (Fig. 3, F and G). Notably, after removal of vacuolin-1, the enlarged lysosomes were progressively restored to their original size, but the recovery rate was not obviously different between the control cells and KO-91 HeLa cells (Fig. 3 H). Taken together, the above findings suggest that loss of WDR91 causes abnormal enlargement of lysosomes by enhancing their fusion.

### Phosphatidylinositol 3-phosphate (PtdIns3P) elevation is not responsible for lysosomal enlargement in the absence of WDR91

WDR91 is a Rab7 effector that couples Rab switching with PtdIns3P down-regulation for early-to-late endosome conversion (Liu et al., 2016; Liu et al., 2017). Loss of WDR91 leads to

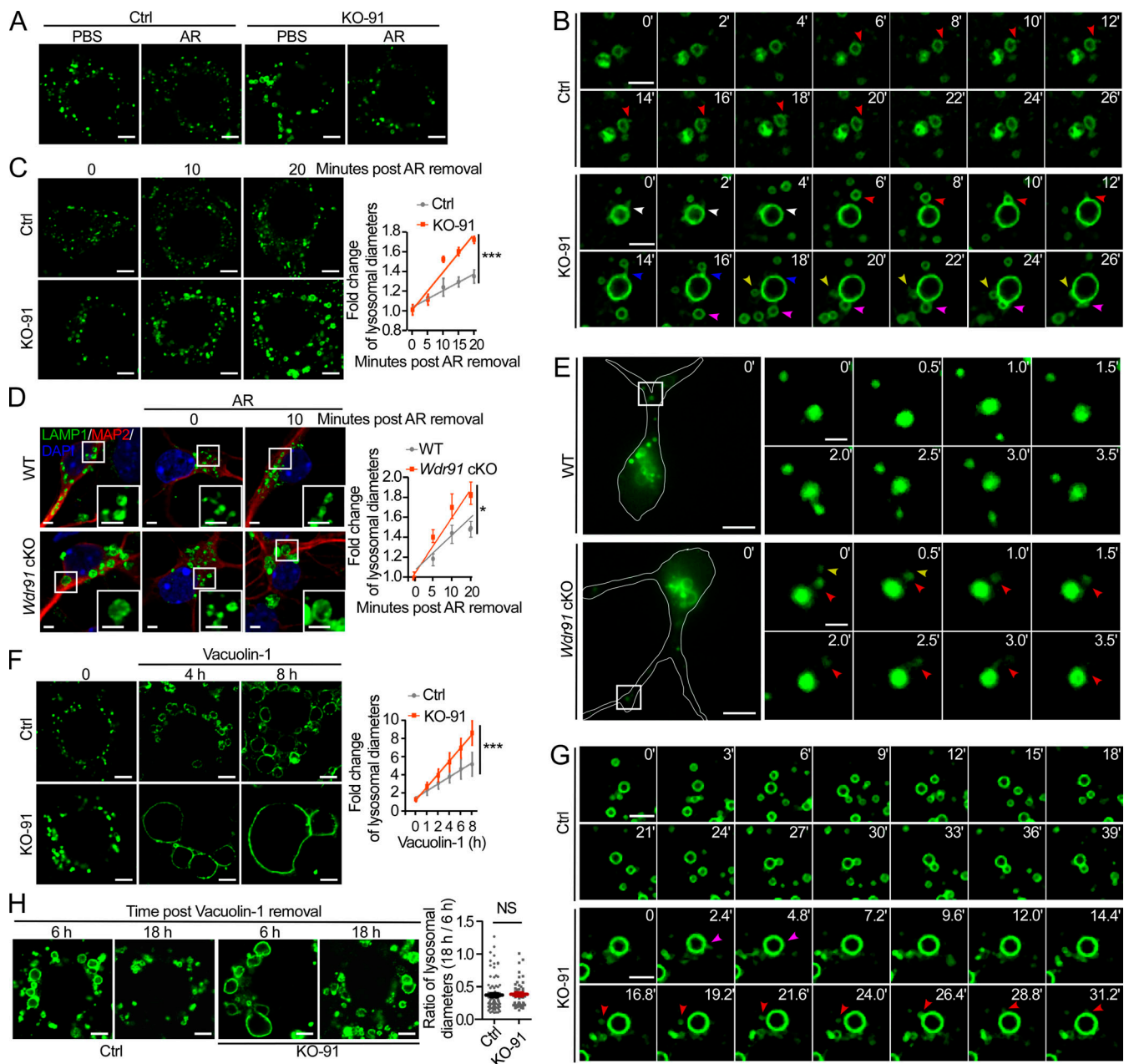


**Figure 3. Loss of WDR91 enhances lysosome fusion.** (A) Immunostaining of LAMP1 in control (Ctrl) and WDR91 knockout (KO-91) HeLa cells treated with PBS or AR for 25 min. Scale bars, 5  $\mu$ m. (B) Time-lapse recording of lysosomal fusion in Ctrl and KO-91 HeLa cells. Cells expressing LAMP1-GFP were treated with AR for 25 min, then returned to normal culture. 0 min refers to the time point when AR was replaced with normal culture medium. Colored arrowheads indicate different vesicles that were followed for fusion. Scale bars, 3  $\mu$ m. (C) Representative images and quantification of lysosomal diameters at the indicated time points after removal of AR. Scale bars, 5  $\mu$ m. Quantification of the change in lysosome diameters is shown on the right.  $\geq 180$  lysosomes from 36 cells were analyzed for each time point. (D) Immunostaining of LAMP1 (green) and Map2 (red) in cultured primary cortex neurons isolated from WT and *Wdr91* cKO mice (left). Nuclei are stained with DAPI (blue). Neurons were treated with AR for 25 min and then returned to normal culture for the indicated time. Scale bars, 2  $\mu$ m. The boxed region is magnified at the bottom right in each image. Scale bars, 2  $\mu$ m. Quantification of lysosomal size during recovery is shown on the right.  $\geq 125$  lysosomes from 25 cells were analyzed for each time point. (E) Time-lapse recording of lysosomal fusion in cultured primary cortex neurons isolated from WT and *Wdr91* cKO mice. Cells expressing LAMP1-GFP were treated with AR for 25 min, then returned to normal culture. 0 min refers to the time point when AR was replaced with normal culture medium. Scale bars, 5  $\mu$ m. The boxed regions of the cells in the left panels were selected for imaging. Time-lapse images are magnified and shown on the right. Scale bars, 1  $\mu$ m. Colored arrowheads indicate different vesicles that were followed. (F) Representative images (left) and quantification (right) of lysosomal sizes in Ctrl and KO-91 HeLa cells at the indicated times after vacuolin-1 was added.  $\geq 160$  lysosomes from 32 cells were analyzed. Scale bars, 5  $\mu$ m. (G) Time-lapse recording of lysosome dynamics in Ctrl and KO-91 HeLa cells treated with 2  $\mu$ M vacuolin-1. Cells expressing LAMP1-GFP were treated with vacuolin-1 for 1 h, then returned to normal culture (time 0) and imaged. Colored arrowheads indicate different vesicles that were followed. Scale bars, 3  $\mu$ m. (H) Representative images (left) and quantification (right) of lysosomal sizes in Ctrl and KO-91 HeLa cells 6 or 18 h following removal of vacuolin-1.  $\geq 225$  lysosomes from 45 cells were analyzed. Scale bars, 5  $\mu$ m. For all quantifications, error bars represent SEM. Data were from three independent experiments. \*,  $P < 0.05$ ; \*\*\*,  $P < 0.001$ .

elevated endosomal PtdIns3P levels that drive the formation of giant intermediate endosomes in HeLa cells and mouse neurons (Liu et al., 2016; Liu et al., 2017). To determine if the increased lysosome fusion ability in KO-91 cells results from elevated endosomal PtdIns3P, we treated cells with VPS34-IN1, a specific inhibitor of the VPS34 PI3K. Whereas VPS34-IN1 inhibited the formation of giant EEA1-positive endosomes in KO-91 HeLa cells, it did not inhibit the enlargement of late endosomes/lysosomes, which stained with LAMP1 and Rab7 (Fig. 4 A). The VPS34-IN1-induced inhibition of EEA1 endosomes was not likely due to impaired biogenesis of the vesicles within the endosome-lysosome pathway, because EEA1 protein levels and LAMP1 staining were unchanged with VPS34-IN1 treatment (Fig. 4 A). Thus, the increased lysosome fusion in the absence of WDR91 was not due to PtdIns3P elevation; instead, this result suggests that WDR91 likely plays a direct role on late endosomes/lysosomes. To investigate this possibility, we first examined whether the lysosomal function of WDR91 requires its interaction with Rab7. In KO-91 HeLa cells, expression of Flag-tagged WT WDR91 significantly reduced the sizes of lysosomes; however, expression of Flag-WDR91(3A) and Flag-WDR91( $\Delta$ 5), two mutants that are unable to interact with Rab7 (Liu et al., 2017), failed to rescue the lysosomal enlargement (Fig. 4 B). In *Wdr91*<sup>-/-</sup> mouse neurons, expression of Flag-WDR91, but not Flag-WDR91(3A) and Flag-WDR91( $\Delta$ 5), similarly rescued the lysosomal enlargement (Fig. 4 C). Thus, WDR91 regulates lysosome homeostasis in a Rab7-dependent manner.

#### WDR91 competes with VPS41 for binding to Rab7

The fusion of late endosomes and lysosomes is dependent on the HOPS complex, which consists of six subunits, VPS11, 16, 18, 33, 39, and 41 (Balderhaar and Ungermann, 2013; Bröcker et al., 2012; Graham et al., 2013). In yeast, Vps39 and 41 directly interact with Ypt7/Rab7, enabling the HOPS complex to tether late endosomes and lysosomes for fusion (Price et al., 2000). Because the lysosomal function of WDR91 requires its interaction with Rab7, we examined whether WDR91 interacts with VPS39 and/or VPS41. In coimmunoprecipitation (coIP) assays, GFP-WDR91 interacted with Flag-VPS39; however, GFP-WDR91 did not interact with Flag-VPS41 (Fig. 5 A). Consistent with this result, mCh-WDR91 formed a complex with GFP-Rab7 and Flag-VPS39 in coIP assays (Fig. 5 B). In contrast, the interaction of Flag-VPS41 with GFP-Rab7 was strongly reduced in the presence of mCh-WDR91 (Fig. 5 C). In addition, we found that the N-terminal WD40-repeat domain of VPS41 (VPS41<sup>1-450</sup>) interacted with GFP-Rab7 in coIP assays, and this domain colocalized to endosomes in HeLa cells (Fig. S4, A–C). In GST pull-down assays, His-tagged VPS41<sup>1-450</sup> directly interacted with GST-Rab7 (Fig. 5 D). In the presence of the WD40-repeat domain of WDR91 (WDR91<sup>392-747</sup>), which also interacted with GST-Rab7, the interaction between VPS41<sup>1-450</sup> and GST-Rab7 was markedly reduced (Fig. 5 D). In contrast, the interaction of endogenous VPS41 with Rab7 was strongly increased in KO-91 HeLa cells in coIP assays (Fig. 5 E). Together, these results suggest that WDR91 likely competes with VPS41 for binding to Rab7. To further prove this hypothesis, we examined the distribution of VPS41, Rab7, and WDR91 on late endosomes/lysosomes. In KO-91 HeLa cells, ~45% of late endosomes/lysosomes displayed overlapping

localization of GFP-VPS41 with mCh-Rab7 (Fig. 5, F and G). When Flag-WDR91 was reintroduced into the KO-91 cells, however, the colocalization of GFP-VPS41 with mCh-Rab7 was greatly reduced; instead, mCh-Rab7 and Flag-WDR91 exhibited overlapping localization on late endosomes/lysosomes (Fig. 5, F and G; and Fig. S4 D). Consistent with these observations, the recruitment of VPS41 to LAMP1-late endosomes/lysosomes was significantly enhanced in both KO-91 HeLa and *Wdr91* cKO mouse neurons compared with control cells (Fig. 5, H and I). Furthermore, the interaction of VPS41 with VPS18 was markedly enhanced (Fig. 5 J), and the colocalization of VPS18 with Rab7 was significantly increased (Fig. 5 K) in KO-91 HeLa cells. Reintroducing Flag-WDR91 strongly inhibited the VPS41-VPS18 interaction (Fig. 5 J). Altogether, these findings demonstrated that WDR91 competes with VPS41 for binding to Rab7, which likely suppresses the assembly of HOPS, thereby preventing excessive late endosomal/lysosomal fusion.

#### Inactivation of VPS41 rescues defects in lysosomes and autophagy caused by WDR91 deficiency

Because WDR91 competes with VPS41 for binding to Rab7, we investigated whether knocking down VPS41 by siRNA or shRNA could rescue the lysosomal enlargement and dysfunction caused by loss of WDR91. In KO-91 HeLa cells, VPS41 siRNA greatly reduced the fusion rate of AR-fragmented lysosomes, which were EEA1-negative and LAMP1-positive, in KO-91 HeLa cells (Fig. S5 A). Consistent with this, the abnormal enlargement of EEA1-negative and LAMP1-positive lysosomes was strongly inhibited by VPS41 siRNA in KO-91 HeLa cells (Fig. 6 A). siRNA of VPS18 or VPS39 similarly reduced lysosomal sizes in KO-91 HeLa cells (Fig. S5 B). The fact that knockdown of different HOPS subunits had a similar rescuing effect on defective lysosomes in KO-91 cells suggests that the rescuing effect of siVPS41 was due to its role as a HOPS component. In *Wdr91* cKO mouse primary neurons, shRNA of *Vps41* similarly decreased the fusion of fragmented lysosomes induced by AR (Fig. S5, C and D), and the lysosomal size, pH, and protease activities, as measured with LysoSensor Blue DND-160 and Magic Red staining, were restored (Fig. 6, B–D). Along with the restoration of lysosome activities, shRNA of *Vps41* significantly reduced the accumulation of autophagic cargoes, including p62 inclusions and LC3 puncta (Fig. 6, E and F).

Finally, we tested if *Vps41* knockdown could rescue the neuron degeneration in *Wdr91* cKO mice. To do so, we stereotactically injected lentivirus coexpressing GFP and *Vps41* shRNA or control shRNA into the cortex of postnatal *Wdr91* cKO mice (Fig. S5 E). *Vps41* shRNA strongly reduced the size of lysosomes (Fig. 7 A) and p62 aggregates (Fig. 7 B) in *Wdr91* cKO mouse brain. Moreover, knockdown of *Vps41* markedly decreased the number of cells positive for AC3 in *Wdr91* cKO mice (Fig. 7 C). Collectively, these findings indicated that reducing HOPS activities by knockdown of *Vps41* rescued the lysosomal defects in the neurons and hence the neuron loss in *Wdr91* cKO mice.

## Discussion

In this study, we revealed that mice lacking *Wdr91* specifically in the central nervous system exhibited behavioral defects,

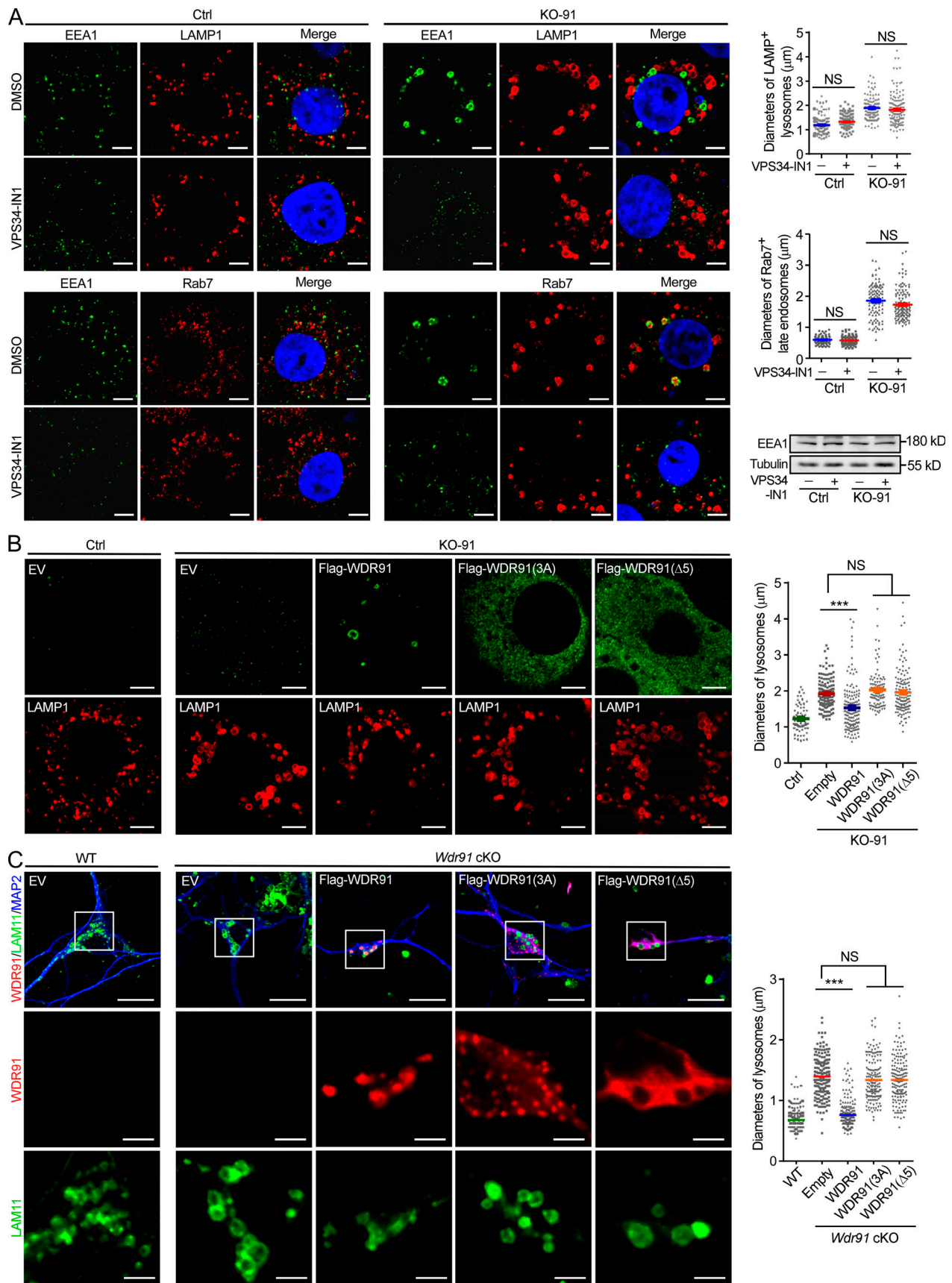


Figure 4. Regulation of lysosomal size by WDR91 depends on its interaction with Rab7. (A) Coimmunostaining of EEA1 with LAMP1 or Rab7 in Ctrl and KO-91 HeLa cells treated without or with VPS34-IN1 (2 μM) for 3 h (left and middle). Scale bars, 5 μm. Quantification of diameters of LAMP1-positive (top right)



and Rab7-positive (middle right) organelles in Ctrl and KO-91 cells is shown on the right.  $\geq 125$  lysosomes from 25 cells were analyzed for each group. Immunoblotting of EEA1 protein levels is shown on the bottom right. **(B)** Coimmunostaining of LAMP1 with WT and mutant WDR91 tagged with Flag in KO-91 HeLa cells (left and middle). Scale bars, 5  $\mu\text{m}$ . Quantification of diameters of LAMP1-positive organelles in KO-91 cells is shown on the right.  $\geq 125$  lysosomes from 25 cells were analyzed for each group. **(C)** Coimmunostaining of LAMP1 (green) and Map2 (blue) with WT and mutant WDR91 tagged with Flag (red) in cultured primary cortex neurons isolated from *Wdr91* cKO mice (left and middle). Scale bars, 20  $\mu\text{m}$ . Boxed regions in the top row are magnified to show WDR91 (middle) and LAMP1 (bottom) staining. Scale bars, 5  $\mu\text{m}$ . Quantification of diameters of LAMP1-positive organelles is shown on the right.  $\geq 125$  lysosomes from 25 cells were analyzed for each group. For all quantifications, error bars represent SEM. Data were from three independent experiments. \*\*\*,  $P < 0.001$ .

including abnormal limb-clasping reflexes and loss of coordinated movement. *Wdr91* deficiency led to marked neuronal loss in the cerebral and cerebellar cortices. These findings suggest that loss of WDR91 causes neuron degeneration. Mechanistically, we demonstrated that loss of WDR91 causes abnormal enlargement and dysfunction of lysosomes, which consequently impairs degradation by the autophagy-lysosome pathway, leading to accumulation of LC3 puncta, p62 aggregates, and ubiquitin-positive inclusions in neurons.

Our results demonstrate that WDR91, as a Rab7 effector, plays an essential role in maintaining lysosome homeostasis. Our previous studies revealed that WDR91 and WDR81 form a complex to interact with the Beclin 1 subunit of the PI3K complex, which inhibits endosomal PtdIns3P synthesis and facilitates early-to-late endosome conversion (Liu et al., 2016). We further found that WDR91 is recruited by active Rab7 to endosomes, thereby coupling endosomal Rab switching with PtdIns3P down-regulation during endosome conversion (Liu et al., 2017). Despite that loss of WDR91 led to formation of abnormally enlarged intermediate endosomes, inhibition of PI3K by VPS34-IN1 abolished the enlargement of intermediate endosomes. This confirms that WDR91 functions in endosome conversion by regulating PtdIns3P levels (Liu et al., 2016; Liu et al., 2017). Loss of WDR91 also led to enlargement of lysosomes (Liu et al., 2016); however, inhibition of PtdIns3P synthesis by VPS34-IN1 did not suppress lysosomal enlargement in KO-91 HeLa cells (Fig. 4 A). This essentially suggests that WDR91 plays a distinct role to regulate late endosomes/lysosomes, which is different from its role in regulating early-to-late endosome conversion. In the nervous system, recent findings revealed that LAMP1 exists on nondegradative endocytic organelles in the axon and dendrite, while in the soma the majority of LAMP1 colocalizes with Rab7, and a substantial proportion of LAMP1 vesicles contain CTSD and other hydrolases (Cheng et al., 2018; Yap et al., 2018). These findings suggest that LAMP1-positive organelles in the soma are mostly late endosomes/lysosomes, although some of them possess no degradative capacity. In the cortical neurons derived from *Wdr91* cKO mice, the large LAMP1-positive organelles were mainly observed in the soma and had very little colocalization with EEA1. This suggests that these LAMP1-positive organelles are late endosomes/lysosomes. Our results suggest that *Wdr91* deficiency-induced lysosomal abnormality and functional impairment is a result of uncontrolled lysosomal fusion. The specific function of WDR91 on late endosomes/lysosomes depends on its interaction with Rab7. WDR91 competes with the VPS41 subunit of the HOPS complex, another Rab7 effector that mediates lysosome fusion, for binding to Rab7. Loss of WDR91 led to an increase in the interaction between Rab7 and VPS41, which

likely promotes lysosomal assembly of the HOPS complex so as to facilitate fusion of lysosomes. The fusion may occur between functional lysosomes and immature ones, leading to lysosomal enlargement, elevation of internal pH, and inefficient processing of lysosomal proteases. In addition, the defective endosome-lysosome transport (Liu et al., 2016; Liu et al., 2017) may contribute to the pH elevation and inefficient processing of lysosomal hydrolases in the absence of WDR91.

In line with the conclusion that loss of WDR91 leads to uncontrolled lysosomal fusion, the fusion of autophagosomes with lysosomes was not affected in *Wdr91*-deficient neurons. As a result, autophagic cargoes were delivered to lysosomes, but not degraded in a timely manner. Our previous studies revealed that *Wdr91* cKO mice were viable and indistinguishable from the control littermates at birth, but they displayed progressive growth retardation and smaller brain size during postnatal development and mostly died at  $\sim 4$  wk of age (Liu et al., 2017). Thus, the neurogenesis in *Wdr91* cKO mice is probably as normal as in WT before birth. Nonetheless, a highly significant increase in AC3 signal was detected in *Wdr91* cKO mouse neurons at P21 (Fig. 1 H). In addition, *Wdr91* cKO mice at P21 had a greatly reduced number of Calbindin-positive Purkinje cells in the cerebellum (Fig. 1 I). Taken together, these results suggest that the accumulated autophagic cargoes probably contributed to neuron degeneration in *Wdr91*-deficient mice. These results, together with our previous findings (Liu et al., 2016; Liu et al., 2017), suggest that WDR91, as a Rab7 effector, has distinct functions on endosomes and lysosomes. On one hand, WDR91 is recruited by active Rab7 to endosomes and forms a complex with WDR81 and the PI3K complex to inhibit endosomal synthesis of PtdIns3P, thus allowing the conversion of early endosomes to late endosomes (Liu et al., 2016; Liu et al., 2017). On the other hand, following recruitment to the late endosomes/lysosomes, WDR91 competes with VPS41 for binding to Rab7, preventing inappropriate fusion of lysosomes. Thus, WDR91 serves as a guardian of lysosomal homeostasis and normal lysosome functions by negatively regulating lysosomal Rab7-HOPS interaction.

The Rab7 GTPase plays a central role in the endolysosome and autophagy-lysosome pathways, which is achieved by interaction of Rab7 with distinct effectors. For example, the Vici syndrome protein EPG5, a Rab7 effector, is recruited to late endosomes/lysosomes by Rab7 and the R-SNAREs VAMP7/8. On the other hand, EPG5 interacts with LC3 and the assembled STX17-SNAP29 Qabc complexes on autophagosomes. Thus, EPG5 determines the fusion specificity of autophagosomes with late endosomes/lysosomes (Wang et al., 2016). Loss of EPG5 leads to nonspecific fusion of autophagosomes with various endocytic vesicles (Wang et al., 2016). *Epg5*-deficient mice exhibit damaged

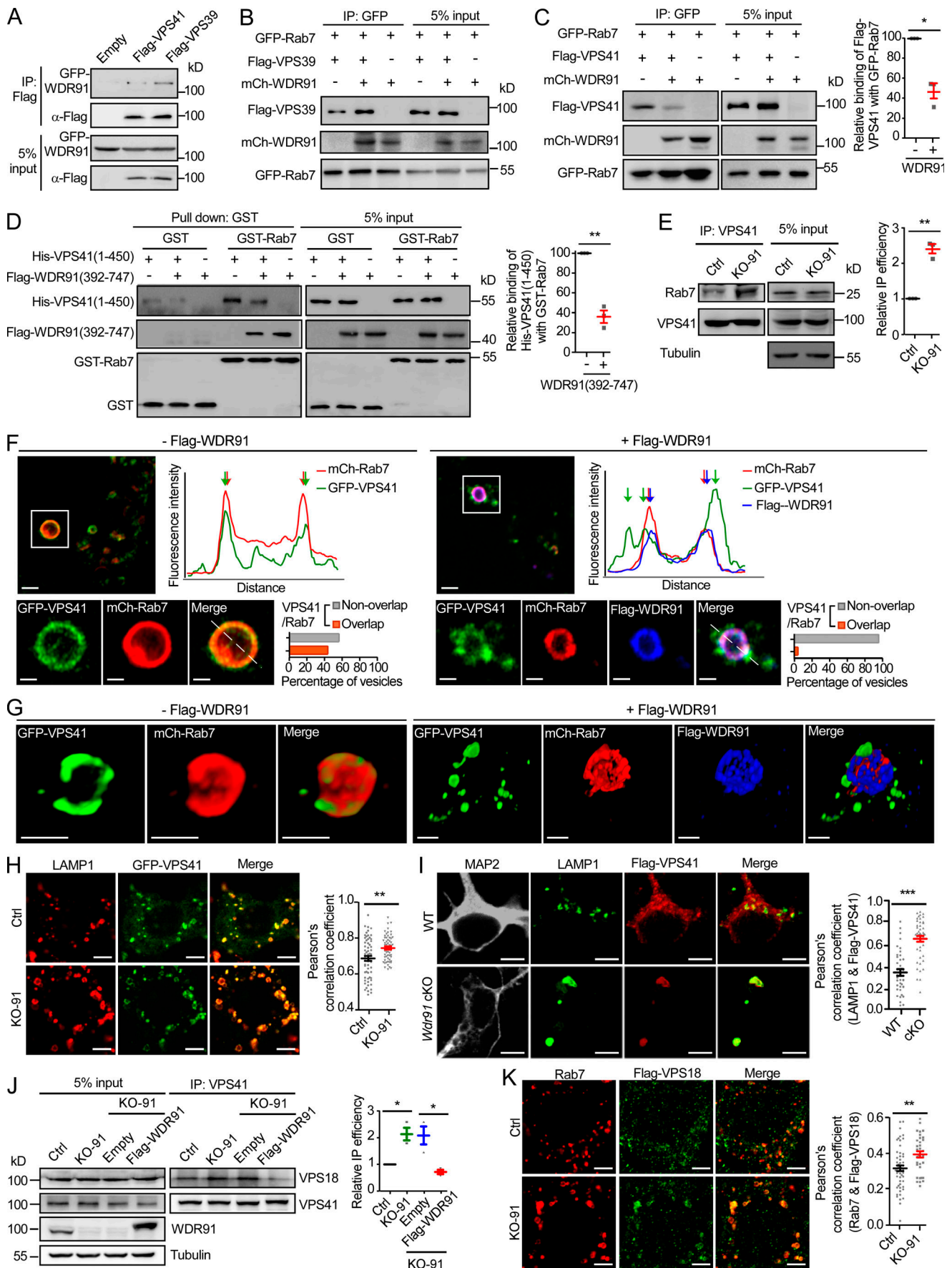


**Figure 5. WDR91 competes with VPS41 for binding to Rab7. (A)** ColP of GFP-WDR91 with Flag-VPS41 and Flag-VPS39. IP was performed with Flag antibody and detected with Flag and GFP antibodies. **(B)** ColP of GFP-Rab7 with Flag-VPS39 and/or mCh-WDR91. IP was performed with GFP antibody and detected with antibodies against GFP, Flag, and mCherry. **(C)** ColP of GFP-Rab7 with Flag-VPS41 and/or mCh-WDR91. IP was performed with GFP antibody and detected with antibodies against GFP, Flag, and mCherry. The relative efficiency of colP of Flag-VPS41 with GFP-Rab7 is quantified and shown on the right. **(D)** Purified GST and GST-Rab7 immobilized on glutathione-Sepharose beads were incubated with purified His-VPS41(1–450), Flag-WDR91(392–747), or both. The precipitated proteins were detected with antibodies against Flag, His, and GST (left). Relative His-VPS41(1–450) pull-down efficiency by GST-Rab7 is quantified and shown in the right panel. **(E)** ColP of endogenous Rab7 with VPS41 in Ctrl or KO-91 HeLa cells. IP was performed with VPS41 antibody and detected with antibodies against the indicated proteins. Quantification of colP efficiency is shown on the right. **(F)** Analysis of vesicular colocalization of GFP-VPS41 with mCh-Rab7 in the absence or presence of Flag-WDR91 in KO-91 HeLa cells. Scale bars, 2  $\mu$ m. Boxed regions are magnified and shown on the right. Fluorescence intensities of mCh-Rab7 (red curve), GFP-VPS41 (green curve), and Flag-WDR91 (blue curve) were measured along the dashed line across the vesicle. Scale bars, 1  $\mu$ m. Quantification of the percentage of vesicles with overlapping mCh-Rab7 and GFP-VPS41 signals. 165 vesicles were examined in >30 cells for each group. **(G)** Representative 3D reconstruction images of vesicular mCh-Rab7 and GFP-VPS41 without or with Flag-WDR91 in KO-91 HeLa cells. Scale bars, 2  $\mu$ m. **(H and I)** Representative images of the colocalization of LAMP1 with GFP-VPS41 (H) or Flag-VPS41 (I) in Ctrl and KO-91 HeLa cells (H) or in cultured primary cortex neurons isolated from WT and *Wdr91* cKO mice (I). Scale bars, 5  $\mu$ m. Quantification of Pearson's correlation coefficient is shown in the right panels.  $\geq 30$  cells were analyzed. **(J)** ColP of endogenous VPS18 with VPS41 in Ctrl or KO-91 HeLa cells. IP was performed with VPS41 antibody and detected with antibodies against the indicated proteins. Quantification of colP efficiency is shown on the right. **(K)** Representative images of the colocalization of Rab7 with Flag-VPS18 in Ctrl and KO-91 HeLa cells. Scale bars, 5  $\mu$ m. Quantification of Pearson's correlation coefficient is shown on the right panel.  $\geq 30$  cells were analyzed for each group. For all quantifications, error bars represent SEM. Data were from three independent experiments. \*,  $P < 0.05$ ; \*\*,  $P < 0.01$ ; \*\*\*,  $P < 0.001$ .

pyramidal neurons and spinal cord motor neurons, owing to failure of autophagosome maturation into degradative autolysosomes (Zhao et al., 2013). In humans, *EPG5* mutations are causative of Vici syndrome, which manifests as a multisystem disorder with defective autophagy (Cullup et al., 2013). In our studies, we revealed that WDR91 acts as a Rab7 effector to play dual functions in endosome conversion (Liu et al., 2016; Liu et al., 2017) and lysosome fusion. Previously we found that mouse neurons deficient in *Wdr91* contain giant intermediate endosomes owing to failure in endosome conversion, which severely impairs the endolysosome pathway (Liu et al., 2017). In this study, we demonstrated that, in addition to its endosomal role, WDR91 is essential to maintain proper fusion of lysosomes by antagonizing the VPS41–Rab7 interaction. Thus, the developmental and neurological defects of *Wdr91*-deficient mice can be attributed to impairment of the endolysosome and autophagy-lysosome pathways. It will be of great interest to investigate if *WDR91* mutations are associated with any human developmental and neurological disorders as well as other diseases.

## Materials and methods

### Antibodies and reagents

The commercial antibodies and reagents used in this paper are listed in Table S1. WDR91 antibody was generated in mice with GST-WDR91(406–730). mCherry antibody was generated in mice by injecting recombinant protein.

### Expression vectors

Mammalian and bacterial expression vectors were constructed by using standard protocols and are listed in Table S2. RFP-GFP-LC3 was provided by L. Yu (Tsinghua University, Beijing, China).

### Mouse strains and behavioral assays

*Wdr91<sup>fl/fl</sup>* and *Wdr91<sup>fl/fl</sup>;nestin-cre* (*Wdr91* cKO) mice were described previously (Liu et al., 2017). For footprint analysis, mouse paws were dipped in nontoxic water-based paints

(forepaws in blue and hindpaws in red). Mice were then allowed to walk down an enclosed runway lined with white paper. Three trials were performed on three separate days within 3 d. For rod tests, mice were placed on a rod rotating at 20 rpm, and the time taken for them to fall from the rod was measured. Three trials were performed on three separate days.

### Cell culture, siRNA, and shRNA treatment

HeLa, HEK293, or N2a cells were cultured at 37°C with 5% CO<sub>2</sub> in DMEM supplemented with 10% FBS (HyClone), 100 U/ml penicillin, and 100 mg/ml streptomycin. Transfections were performed with Lipofectamine 2000 (Invitrogen) according to the manufacturer's instructions. siRNA was achieved by transfection of oligonucleotides listed in Table S3.

### Isolation, culture, and transfection of primary hippocampal neurons

Cortex neurons were isolated from *Wdr91<sup>fl/fl</sup>* or *Wdr91<sup>fl/fl</sup>;nestin-cre* (*Wdr91* cKO) P0 mice. In brief, the brain cortex was microdissected in ice-cold HBSS (Gibco) and incubated in 0.05% trypsin-EDTA (Invitrogen) for 15 min at RT. Viable cells were seeded on poly-L-lysine-coated 6- or 12-multiwell plates. The dispersed cortex neurons were cultured at 37°C with 5% CO<sub>2</sub> in neurobasal medium (Invitrogen) supplemented with 2% B27, 0.5 mM L-glutamine, and 1% antibiotics. Cortex neurons were transfected 4 d after isolation. 1  $\mu$ g of total DNA and 1  $\mu$ l of Lipofectamine 2000 reagent that was diluted in Opti-MEM medium (Gibco) were used per well in a 24-well plate. The neurons were fixed for analysis 72 h after transfection.

### Immunostaining

HeLa cells or cultured hippocampus neurons grown on glass-bottom dishes (NEST) were fixed in 4% PFA followed by permeabilization with 0.5% saponin for 10 min. After extensive washing with PBS, cells were incubated in blocking buffer (5% BSA, 0.25% saponin, and PBS) for 1 h at RT and then incubated with primary antibodies in blocking buffer at 4°C overnight. Cells were washed extensively again and incubated with Alexa Fluor 488-, 568-, or 647-conjugated secondary antibodies in

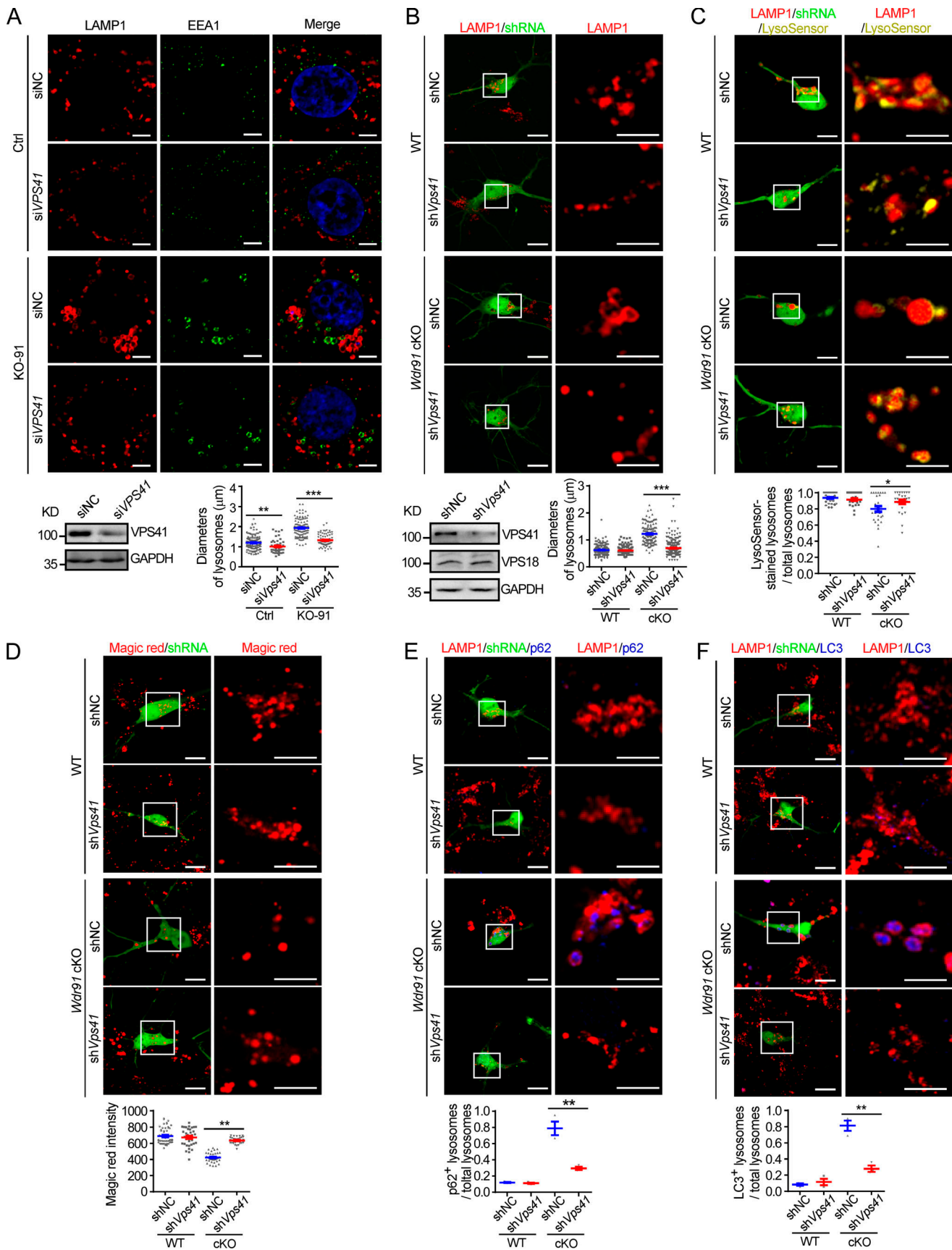


Figure 6. **VPS41 knockdown ameliorates the lysosomal and autophagic defects caused by WDR91 deficiency.** (A) Immunostaining of LAMP1 and EEA1 (top) and quantification of lysosome (EEA-1<sup>+</sup>/LAMP1<sup>+</sup>) sizes (bottom right) in Ctrl and KO-91 HeLa cells treated with negative control siRNA (siNC) or VPS41

siRNA (siVPS41) for 72 h. Scale bars, 5  $\mu$ m.  $\geq$ 125 lysosomes from 25 cells were analyzed for each group. Immunoblotting of VPS41 in HeLa cells treated with siNC and siVPS41 for 72 h is shown on the bottom left. **(B)** Representative images (top) and quantification of lysosome size (bottom right) in WT or *Wdr91* cKO primary neurons coexpressing LAMP1-RFP with negative control shRNA (shNC) or *Vps41* shRNA (shVps41). GFP was used as transfection marker. Scale bars, 10  $\mu$ m. Boxed regions in the left column are magnified on the right to show LAMP1 staining. Scale bars, 5  $\mu$ m.  $\geq$ 150 lysosomes from 25 cells were analyzed for each group. Immunoblotting of VPS41 and VPS18 in N2a cells treated with shNC or shVps41 for 72 h is shown on the bottom left. **(C)** LysoSensor staining in WT and *Wdr91* cKO primary neurons coexpressing LAMP1-RFP with shNC or shVps41 (left). GFP was used as transfection marker. Scale bars, 10  $\mu$ m. Boxed regions in the left column are magnified on the right to show LAMP1 (red) and LysoSensor (yellow) staining. Scale bars, 5  $\mu$ m. The ratio of LysoSensor-stained lysosomes to total lysosomes in a cell is quantified and shown on the bottom.  $\geq$ 22 cells were analyzed for each group. **(D–F)** Staining of Magic Red (D), p62 with LAMP1 (E), and LC3 with LAMP1 (F) in WT or *Wdr91* cKO primary neurons treated with shNC or shVps41. GFP was used as transfection marker. Scale bars, 10  $\mu$ m. In each panel, boxed regions in the left column are magnified on the right to show staining of indicated proteins. Scale bars, 5  $\mu$ m. Indicated quantifications are shown on the bottom. In D,  $\geq$ 35 cells were analyzed for each group. In E and F,  $\geq$ 48 cells were analyzed for each group. For all quantifications, error bars represent SEM. Data were from three independent experiments. \*,  $P < 0.05$ ; \*\*,  $P < 0.01$ ; \*\*\*,  $P < 0.001$ .

blocking buffer for 1 h at RT. After another round of extensive washing, cells were ready for confocal microscopy analysis.

### Staining of brain sections

Mice were anesthetized and transcardially perfused with saline followed by 4% PFA. For H&E staining, the brains were dehydrated sequentially in graded ethanol (70, 80, and 95% for 1 h each, followed by 100% ethanol for 1 h, three times) and cleared in xylene for 1 h with two repeats. The brains were then immersed in paraffin for 1 h with three repeats and sectioned at 8  $\mu$ m on a microtome. The sections were deparaffinized with xylene and rehydrated by sequential incubation in graded ethanol (100, 100, 95, 80, 70, and 50%, each for 5 min). The sections were stained with 1 $\times$  hematoxylin for 18 min, washed with distilled water for 3 s and acid alcohol for 2 s, and then rinsed with distilled water for 14 min. After staining with 0.5% eosin for 70 s, the sections were washed with 100% ethanol for 2 min with three repeats and xylene for 2 min with three repeats and finally mounted for microscopy analysis. For immunofluorescence staining, the brains were subjected to cryosectioning. In brief, the fixed brains were dehydrated in 30% sucrose for 48 h and frozen in 30% sucrose. Brain sections (40- $\mu$ m thickness) were generated using a sliding microtome equipped with a  $-20^{\circ}\text{C}$  freezer and transferred into 96-well plates filled with cryoprotectant solution (glycerol, ethylene glycol, and 0.1 M phosphate buffer, pH 7.4, 1:1:2 by volume). After extensive washing with PBS, the sections were incubated in blocking buffer (5% donkey serum, 0.25% Triton X-100, and PBS) for 1 h and then incubated with primary antibodies in blocking buffer at  $4^{\circ}\text{C}$  overnight. The sections were washed extensively again and incubated with Alexa Fluor 488-, 568-, or 647-conjugated secondary antibodies in blocking buffer for 2 h. The sections were mounted, coverslipped, and maintained at  $4^{\circ}\text{C}$  in the dark until analysis.

### Lysosome assays

Cortex neurons seeded on a confocal dish (Glass Bottom Dish; In Vitro Scientific) were incubated with 1  $\mu\text{M}$  LysoSensor Yellow/Blue DND-160 (Invitrogen) at  $37^{\circ}\text{C}$  for 30 min, washed twice with medium, and live-imaged immediately at  $37^{\circ}\text{C}$ . Cells were excited at 405 nm, and images were taken of the emission at 540 nm for yellow fluorescence. To evaluate lysosomal enzyme activities, cells were incubated with Pepstatin A-BODIPY FL Conjugate and Magic Red according to the manufacturer's instructions. The cells were washed and visualized with a Zeiss

LSM880 Laser Scanning Confocal microscope. To assess the change of lysosome sizes, the diameters of the five largest lysosomes were determined in individual cells.

### Microscopy

Fluorescent images were obtained with an inverted confocal microscope system (LSM880; Zeiss) coupled with a camera using a  $100\times$  1.42-NA oil objective. Excitation was achieved using 405-, 488-, 560-, and 633-nm lasers. All images were taken at RT and processed with Zen Blue 2 software (Zeiss). The integrated fluorescence intensity of each channel of interest and Pearson's correlation coefficient were determined with the same software. The 3D structure of vesicles was constructed with 47 Z-section images (100 nm/section) captured with Zeiss Airyscan. Z-series images were processed with Airyscan processing and projected using the transparency option in Zen blue 2 software (Zeiss) or the maximum-intensity projection option in Imaris software (Oxford Instruments).

To monitor the dynamics of lysosomes, HeLa cells were grown on a glass-bottom dish (NEST) and transfected with LAMP1-GFP. 24 h later, cells were imaged at an excitation wavelength of 488 nm. The images were exported, and a video was created with Picture2avi (Anton Small).

### TEM

Perfused mouse brains were fixed for 2 h or overnight at  $4^{\circ}\text{C}$  with 0.1 M PBS containing 4% PFA and 2.5% glutaraldehyde at P21. Cultured cortex neurons at 6 d in vitro were fixed for 2 h at  $4^{\circ}\text{C}$  with 0.1 M PBS containing 2.5% glutaraldehyde. The samples were further treated sequentially with 1%  $\text{OsO}_4$  for 2 h and 2% uranyl acetate overnight at  $4^{\circ}\text{C}$ . Samples were dehydrated by sequential incubation with an acetone series (30, 50, 70, 80, 90, 95, 100, 100, and 100%, 10 min each) and infiltrated with SPI-Pon 812 resin (resin/acetone 1:3 for 3 h, 1:1 for 5 h, 3:1 overnight, 100% resin for 12 h, and 100% resin for 12 h). The samples were embedded at  $60^{\circ}\text{C}$  for 48 h and cut into 70-nm sections with a microtome EM UC7 (Leica Biosystems). Sections were observed with TEM (JEM-1400 JEOL Japan) operated at 80 kV, and digital images were captured with a  $4\text{K} \times 2.7\text{K}$ -pixel charge-coupled device camera (Gatan).

### Lysosomal fusion and fission assays

HeLa cells or primary neurons were incubated in AR (80 mM NaCl, 70 mM sodium acetate, 5 mM KCl, 2 mM  $\text{CaCl}_2$ , 1 mM  $\text{MgCl}_2$ , 2 mM  $\text{NaH}_2\text{PO}_4$ , 10 mM Hepes, 10 mM glucose, and

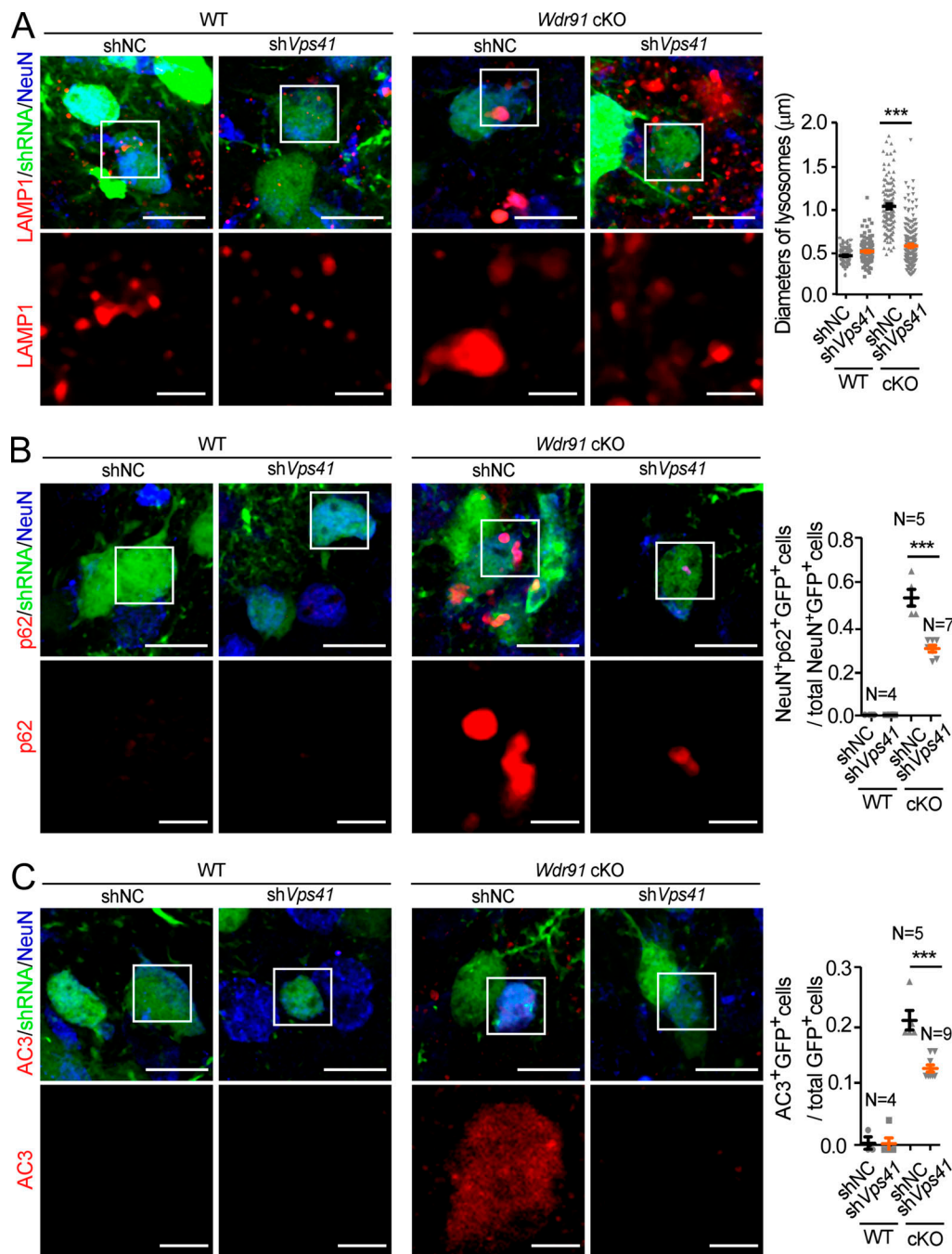


Figure 7. **VPS41 knockdown rescues the neuron degeneration in *Wdr91* cKO mice.** (A) Staining of LAMP1 (red) and NeuN (blue) in brain cortex of WT or *Wdr91* cKO mice injected with lentivirus coexpressing GFP and *Vps41* shRNA or control shRNA constructs. Scale bars, 10  $\mu$ m. Boxed regions are magnified on the bottom to show LAMP1 staining. Scale bars, 2  $\mu$ m. Quantification of diameters of LAMP1-positive organelles is shown on the right.  $\geq 120$  lysosomes from 24 cells from three mice were analyzed for each group. (B) Staining of p62 (red) and NeuN (blue) in brain cortex of WT or *Wdr91* cKO mice injected with lentivirus coexpressing GFP and *Vps41* shRNA or control shRNA constructs. Scale bars, 10  $\mu$ m. Boxed regions are magnified on the bottom to show p62 staining. Scale bars, 2  $\mu$ m. Quantification of p62-positive cells is shown on the right.  $\geq 48$  cells were analyzed for each group. (C) Staining of AC3 (red) and NeuN (blue) in brain cortex of WT or *Wdr91* cKO mice injected with lentivirus coexpressing GFP and *Vps41* shRNA or control shRNA constructs. Scale bars, 10  $\mu$ m. Boxed regions are magnified on the bottom to show AC3 staining. Scale bars, 2  $\mu$ m. Quantification of AC3-positive cells is shown on the right.  $\geq 59$  cells were analyzed for each group. For all quantifications, error bars represent SEM. Data were from three independent experiments. \*\*,  $P < 0.01$ ; \*\*\*,  $P < 0.001$ .

0.5 mg/ml BSA, pH 6.9; Heuser, 1989) for 25 min at 37°C and replaced with normal culture medium. For vacuolin-1 treatment, cells were incubated in normal culture medium containing 2  $\mu$ M vacuolin-1 (Cerny et al., 2004) for the indicated time. For

recovery assays, cells were incubated with 2  $\mu$ M vacuolin-1 for 1 h, washed twice with culture medium, and further cultured in normal growth medium for 6 or 18 h. Cells were imaged as described above.

### Real-time quantitative PCR (qPCR) and Western blotting

Total RNA was prepared with Trizol, and cDNA was synthesized with the Maloney murine leukemia virus reverse transcription according to the manufacturer's instructions. The relative mRNA expression levels were quantified by real-time qPCR and normalized to the *GAPDH* mRNA level. For Western blotting, HeLa cells, brain tissues, or cortex neurons were lysed in ice-cold radioimmunoprecipitation assay buffer (20 mM Tris-HCl, pH 7.5, 100 mM NaCl, 0.1% SDS, 0.5% sodium deoxycholate, and 1 mM PMSF) containing Complete Protease Inhibitor Cocktail (Roche). Brain tissues were homogenized and sonicated, and the homogenates were spun down at 12,000 rpm for 10 min at 4°C. 50 µg of total proteins in the supernatants were resolved on SDS-PAGE, blotted, and probed with the indicated antibodies. β-Actin, GAPDH, or Tubulin was used as the loading control. Quantification of Western blots was performed using ImageJ software (National Institutes of Health).

### Immunoprecipitation (IP)

Cells were washed twice with ice-cold PBS and extracted with lysis buffer (20 mM Tris-HCl, pH 7.5, 150 mM NaCl, 10 mM MgCl<sub>2</sub>, 1% Triton X-100, and protease inhibitor cocktail). Cell lysates were incubated with GFP-Trap beads (ChromoTek) or Flag-Trap beads (Sigma-Aldrich) overnight at 4°C. Bound proteins were washed three times with wash buffer (20 mM Tris-HCl, pH 7.5, 200 mM NaCl, 10 mM MgCl<sub>2</sub>, 0.1% NP-40, and protease inhibitor cocktail) and resolved on SDS-PAGE for immunoblotting. For IP of endogenous proteins, cell lysates were incubated at 4°C overnight with protein G-agarose beads preloaded with VPS41 antibody. After extensive washing, the precipitated proteins were detected with Western blotting.

### Recombinant proteins and GST pull-down

Recombinant GST-Rab7, His-VPS41(1–450), and Flag-WDR91(392–747) proteins were expressed in BL21 (Rosetta) bacterial cells and purified with glutathione-Sepharose beads (GE), His beads (GE), or Flag beads (Sigma-Aldrich), respectively, according to the instructions provided by the supplier. Purified GST-tagged proteins (2.5 µg) were immobilized on glutathione-Sepharose beads and incubated with His-VPS41(1–450) or Flag-WDR91(392–747) or both in binding buffer (25 mM Tris-HCl, pH 8.8, 150 mM NaCl, 5 mM MgCl<sub>2</sub>, 0.1% NP-40, 1 mM PMSF, and protease inhibitor cocktail) at 4°C overnight. After extensive washing with wash buffer (25 mM Tris-HCl, pH 8.8, 200 mM NaCl, 0.3% NP-40, and 1 mM PMSF), bound proteins were detected by Western blotting.

### Statistical analysis

Statistical analyses were performed using Prism (GraphPad Software) to generate curves or bar graphs. All error bars represent SEM. Two-tailed unpaired *t* test was used for statistical analysis of two groups of samples. One-way ANOVA was used to evaluate the statistical significance of multiple groups of samples. \*, *P* < 0.05; \*\*, *P* < 0.01; and \*\*\*, *P* < 0.001. *P* > 0.05 was considered not significant (NS). Data distribution was assumed to be normal, but this was not formally tested.

### Online supplemental material

Fig. S1 characterizes brain defects of *Wdr91* cKO mice. Fig. S2 analyzes accumulation of autophagic cargoes in *Wdr91* cKO mouse brain. Fig. S3 analyzes lysosomal dynamics after AR treatment. Fig. S4 characterizes the interaction of VPS41 with Rab7. Fig. S5 analyzes the effect of VPS41 knockdown on abnormal lysosomal fusion caused by loss of WDR91. Table S1 lists the antibodies and reagents used in the study. Table S2 lists the expression vectors used in the study. Table S3 lists the oligonucleotides used for siRNA and shRNA in the study.

### Acknowledgments

We thank Dr. I. Hanson for proofreading the manuscript.

This research was supported by the National Natural Science Foundation of China (91954204 and 31730053 to C. Yang; 81571099 and 31771123 to W. Guo), the National Basic Research Program of China (2017YFA0503403 to C. Yang and 2019YFA080200 to W. Guo), Yunnan Provincial Science and Technology Department (202001BB050077 to C. Yang), Chinese Academy of Sciences (QYZDB-SSW-SMC046 to W. Guo), and Beijing Brain Project (Z16110000266004 to W. Guo).

The authors declare no competing financial interests.

Author contributions: C. Yang and W. Guo conceived and supervised the research. R. Xing did most of the neuronal experiments. H. Zhou did most cell biological and protein interaction experiments. Y. Jian performed EM analysis. L. Li, M. Wang, N. Liu, Q. Yin, and Z. Liang contributed experimental materials. C. Yang, W. Guo, and H. Zhou wrote the manuscript with feedback from all authors.

Submitted: 11 July 2020

Revised: 22 February 2021

Accepted: 5 May 2021

### References

- Balderhaar, H.J.K., and C. Ungermann. 2013. CORVET and HOPS tethering complexes - coordinators of endosome and lysosome fusion. *J. Cell Sci.* 126:1307–1316. <https://doi.org/10.1242/jcs.107805>
- Balderhaar, H.J.K., H. Arlt, C. Ostrowicz, C. Bröcker, F. Sündermann, R. Brandt, M. Babst, and C. Ungermann. 2010. The Rab GTPase Ypt7 is linked to retromer-mediated receptor recycling and fusion at the yeast late endosome. *J. Cell Sci.* 123:4085–4094. <https://doi.org/10.1242/jcs.071977>
- Ballabio, A., and J.S. Bonifacino. 2020. Lysosomes as dynamic regulators of cell and organismal homeostasis. *Nat. Rev. Mol. Cell Biol.* 21:101–118. <https://doi.org/10.1038/s41580-019-0185-4>
- Bröcker, C., A. Kuhlee, C. Gatsogiannis, H.J.K. Balderhaar, C. Hönscher, S. Engelbrecht-Vandré, C. Ungermann, and S. Raunser. 2012. Molecular architecture of the multisubunit homotypic fusion and vacuole protein sorting (HOPS) tethering complex. *Proc. Natl. Acad. Sci. USA.* 109:1991–1996. <https://doi.org/10.1073/pnas.1117797109>
- Cai, Q., L. Lu, J.H. Tian, Y.B. Zhu, H. Qiao, and Z.H. Sheng. 2010. Snapin-regulated late endosomal transport is critical for efficient autophagy-lysosomal function in neurons. *Neuron.* 68:73–86. <https://doi.org/10.1016/j.neuron.2010.09.022>
- Cecconi, F., and B. Levine. 2008. The role of autophagy in mammalian development: cell makeover rather than cell death. *Dev. Cell.* 15:344–357. <https://doi.org/10.1016/j.devcel.2008.08.012>
- Cerny, J., Y. Feng, A. Yu, K. Miyake, B. Boronovo, J. Klumperman, J. Meldolesi, P.L. McNeil, and T. Kirchhausen. 2004. The small chemical vacuolin-1 inhibits Ca(2+)-dependent lysosomal exocytosis but not cell

- resealing. *EMBO Rep.* 5:883–888. <https://doi.org/10.1038/sj.embor.7400243>
- Cheng, X.T., Y.X. Xie, B. Zhou, N. Huang, T. Farfel-Becker, and Z.H. Sheng. 2018. Characterization of LAMP1-labeled nondegradative lysosomal and endocytic compartments in neurons. *J. Cell Biol.* 217:3127–3139. <https://doi.org/10.1083/jcb.201711083>
- Chou, H.T., D. Dukovski, M.G. Chambers, K.M. Reinisch, and T. Walz. 2016. CATCHR, HOPS and CORVET tethering complexes share a similar architecture. *Nat. Struct. Mol. Biol.* 23:761–763. <https://doi.org/10.1038/nsm.3264>
- Cullup, T., A.L. Kho, C. Dionisi-Vici, B. Brandmeier, F. Smith, Z. Urry, M.A. Simpson, S. Yau, E. Bertini, V. McClelland, et al. 2013. Recessive mutations in EPG5 cause Vici syndrome, a multisystem disorder with defective autophagy. *Nat. Genet.* 45:83–87. <https://doi.org/10.1038/ng.2497>
- Dehay, B., A. Ramirez, M. Martinez-Vicente, C. Perier, M.H. Canron, E. Doudnikoff, A. Vital, M. Vila, C. Klein, and E. Bezard. 2012. Loss of P-type ATPase ATP13A2/PARK9 function induces general lysosomal deficiency and leads to Parkinson disease neurodegeneration. *Proc. Natl. Acad. Sci. USA.* 109:9611–9616. <https://doi.org/10.1073/pnas.1112368109>
- Durchfort, N., S. Verhoef, M.B. Vaughn, R. Shrestha, D. Adam, J. Kaplan, and D.M. Ward. 2012. The enlarged lysosomes in beige j cells result from decreased lysosome fission and not increased lysosome fusion. *Traffic.* 13:108–119. <https://doi.org/10.1111/j.1600-0854.2011.01300.x>
- Farfel-Becker, T., J.C. Roney, X.T. Cheng, S. Li, S.R. Cuddy, and Z.H. Sheng. 2019. Neuronal Soma-Derived Degradative Lysosomes Are Continuously Delivered to Distal Axons to Maintain Local Degradation Capacity. *Cell Rep.* 28:51–64.e4. <https://doi.org/10.1016/j.celrep.2019.06.013>
- Graham, S.C., L. Wartosch, S.R. Gray, E.J. Scourfield, J.E. Deane, J.P. Luzio, and D.J. Owen. 2013. Structural basis of Vps33A recruitment to the human HOPS complex by Vps16. *Proc. Natl. Acad. Sci. USA.* 110:13345–13350. <https://doi.org/10.1073/pnas.1307074110>
- Heuser, J. 1989. Changes in lysosome shape and distribution correlated with changes in cytoplasmic pH. *J. Cell Biol.* 108:855–864. <https://doi.org/10.1083/jcb.108.3.855>
- Krämer, L., and C. Ungermann. 2011. HOPS drives vacuole fusion by binding the vacuolar SNARE complex and the Vam7 PX domain via two distinct sites. *Mol. Biol. Cell.* 22:2601–2611. <https://doi.org/10.1091/mbc.e11-02-0104>
- Kuhlee, A., C. Gatsogiannis, C. Broecker, C. Ungermann, and S. Raunser. 2013. HOPS - Molecular Insights into Vesicle Sorting. *Biophys. J.* 104(Suppl. 1): 650a. <https://doi.org/10.1016/j.bpj.2012.11.3589>
- Langemeyer, L., F. Fröhlich, and C. Ungermann. 2018. Rab GTPase Function in Endosome and Lysosome Biogenesis. *Trends Cell Biol.* 28:957–970. <https://doi.org/10.1016/j.tcb.2018.06.007>
- Lenk, G.M., C.J. Ferguson, C.Y. Chow, N. Jin, J.M. Jones, A.E. Grant, S.N. Zolov, J.J. Winters, R.J. Giger, J.J. Dowling, et al. 2011. Pathogenic mechanism of the FIG4 mutation responsible for Charcot-Marie-Tooth disease CMT4j. *PLoS Genet.* 7:e1002104. <https://doi.org/10.1371/journal.pgen.1002104>
- Levine, B., and D.J. Klionsky. 2004. Development by self-digestion: molecular mechanisms and biological functions of autophagy. *Dev. Cell.* 6:463–477. [https://doi.org/10.1016/S1534-5807\(04\)00099-1](https://doi.org/10.1016/S1534-5807(04)00099-1)
- Lin, X.S., T. Yang, S.C. Wang, Z. Wang, Y. Yun, L.X. Sun, Y.H. Zhou, X.H. Xu, C. Akazawa, W.J. Hong, and T.L. Wang. 2014. RILP interacts with HOPS complex via VPS41 subunit to regulate endocytic trafficking. *Sci. Rep.* 4: 7282.
- Liu, K., Y.L. Jian, X.J. Sun, C.K. Yang, Z.Y. Gao, Z.L. Zhang, X.Z. Liu, Y. Li, J. Xu, Y.D. Jing, et al. 2016. Negative regulation of phosphatidylinositol 3-phosphate levels in early-to-late endosome conversion. *J. Cell Biol.* 212: 181–198.
- Liu, K., R. Xing, Y. Jian, Z. Gao, X. Ma, X. Sun, Y. Li, M. Xu, X. Wang, Y. Jing, et al. 2017. WDR91 is a Rab7 effector required for neuronal development. *J. Cell Biol.* 216:3307–3321. <https://doi.org/10.1083/jcb.201705151>
- Lürick, A., D. Kümmel, and C. Ungermann. 2018. Multisubunit tethers in membrane fusion. *Curr. Biol.* 28:R417–R420. <https://doi.org/10.1016/j.cub.2017.12.012>
- McEwan, D.G., D. Popovic, A. Gubas, S. Terawaki, H. Suzuki, D. Stadel, F.P. Coxon, D. Miranda de Stegmann, S. Bhogaraju, K. Maddi, et al. 2015a. PLEKHM1 regulates autophagosome-lysosome fusion through HOPS complex and LC3/GABARAP proteins. *Mol. Cell.* 57:39–54. <https://doi.org/10.1016/j.molcel.2014.11.006>
- McEwan, D.G., B. Richter, B. Claudi, C. Wigge, P. Wild, H. Farhan, K. McGourty, F.P. Coxon, M. Franz-Wachtel, B. Perdu, et al. 2015b. PLEKHM1 regulates Salmonella-containing vacuole biogenesis and infection. *Cell Host Microbe.* 17:58–71. <https://doi.org/10.1016/j.chom.2014.11.011>
- Orr, M.E., and S. Oddo. 2013. Autophagic/lysosomal dysfunction in Alzheimer's disease. *Alzheimers Res. Ther.* 5:53. <https://doi.org/10.1186/alzrt217>
- Pan, T., S. Kondo, W. Le, and J. Jankovic. 2008. The role of autophagy-lysosome pathway in neurodegeneration associated with Parkinson's disease. *Brain.* 131:1969–1978. <https://doi.org/10.1093/brain/awm318>
- Price, A., D. Seals, W. Wickner, and C. Ungermann. 2000. The docking stage of yeast vacuole fusion requires the transfer of proteins from a cis-SNARE complex to a Rab/Ypt protein. *J. Cell Biol.* 148:1231–1238. <https://doi.org/10.1083/jcb.148.6.1231>
- Ramirez, A., A. Heimbach, J. Gründemann, B. Stiller, D. Hampshire, L.P. Cid, I. Goebel, A.F. Mubaidin, A.L. Wriekat, J. Roeper, et al. 2006. Hereditary parkinsonism with dementia is caused by mutations in ATP13A2, encoding a lysosomal type 5 P-type ATPase. *Nat. Genet.* 38:1184–1191. <https://doi.org/10.1038/ng1884>
- Rocznik-Ferguson, A., C.S. Petit, F. Froehlich, S. Qian, J. Ky, B. Angarola, T.C. Walther, and S.M. Ferguson. 2012. The transcription factor TFEB links mTORC1 signaling to transcriptional control of lysosome homeostasis. *Sci. Signal.* 5:ra42. <https://doi.org/10.1126/scisignal.2002790>
- Wang, M., C. Tang, R. Xing, X. Liu, X. Han, Y. Liu, L. Wang, C. Yang, and W. Guo. 2021. WDR81 regulates adult hippocampal neurogenesis through endosomal SARA-TGFβ signaling. *Mol. Psychiatry.* 26:694–709. <https://doi.org/10.1038/s41380-018-0307-y>
- Wang, Z., G. Miao, X. Xue, X. Guo, C. Yuan, Z. Wang, G. Zhang, Y. Chen, D. Feng, J. Hu, and H. Zhang. 2016. The Vici Syndrome Protein EPG5 is a Rab7 Effector that Determines the Fusion Specificity of Autophagosomes with Late Endosomes/Lysosomes. *Mol. Cell.* 63:781–795. <https://doi.org/10.1016/j.molcel.2016.08.021>
- Winckler, B., V. Faundez, S. Maday, Q. Cai, C. Guimas Almeida, and H. Zhang. 2018. The Endolysosomal System and Proteostasis: From Development to Degeneration. *J. Neurosci.* 38:9364–9374. <https://doi.org/10.1523/JNEUROSCI.1665-18.2018>
- Yap, C.C., and B. Winckler. 2012. Harnessing the power of the endosome to regulate neural development. *Neuron.* 74:440–451. <https://doi.org/10.1016/j.neuron.2012.04.015>
- Yap, C.C., L. Digilio, L.P. McMahon, A.D.R. Garcia, and B. Winckler. 2018. Degradation of dendritic cargos requires Rab7-dependent transport to somatic lysosomes. *J. Cell Biol.* 217:3141–3159. <https://doi.org/10.1083/jcb.201711039>
- Yu, L., C.K. McPhee, L. Zheng, G.A. Mardones, Y. Rong, J. Peng, N. Mi, Y. Zhao, Z. Liu, F. Wan, et al. 2010. Termination of autophagy and reformation of lysosomes regulated by mTOR. *Nature.* 465:942–946. <https://doi.org/10.1038/nature09076>
- Zhao, H., Y.G. Zhao, X. Wang, L. Xu, L. Miao, D. Feng, Q. Chen, A.L. Kovács, D. Fan, and H. Zhang. 2013. Mice deficient in Epg5 exhibit selective neuronal vulnerability to degeneration. *J. Cell Biol.* 200:731–741. <https://doi.org/10.1083/jcb.201211014>



## Supplemental material

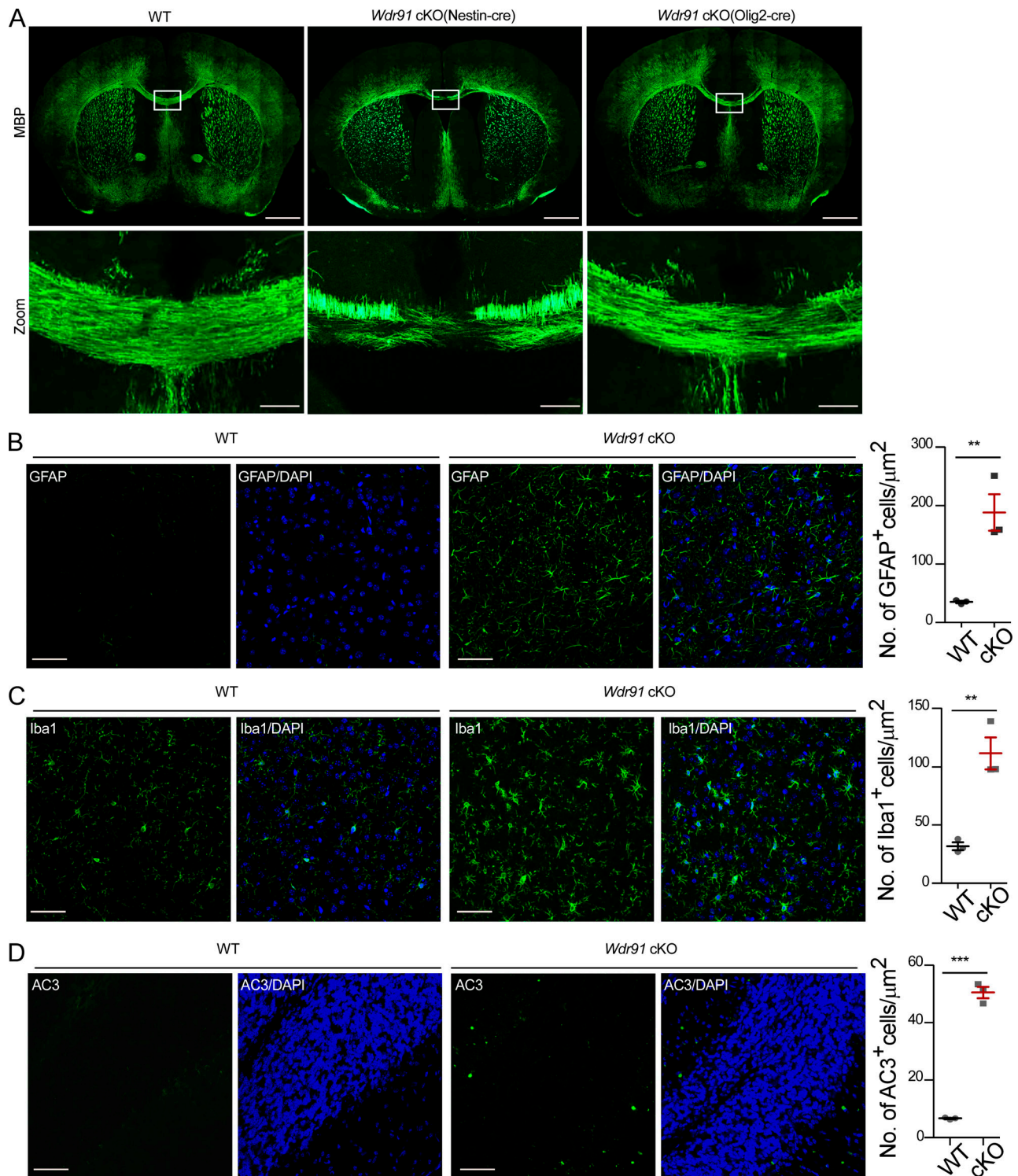


Figure S1. **Loss of WDR91 leads to neuron degeneration.** (A) Immunostaining of MBP in *Wdr91<sup>f/f</sup>*, *Wdr91<sup>f/f</sup>* Nestin cre and *Wdr91<sup>f/f</sup>* Olig2 cre mice at P21. Scale bars, 1,000  $\mu\text{m}$ . Boxed regions in each image are magnified on the bottom to show the corpus callosum. Scale bars, 100  $\mu\text{m}$ . (B–D) Immunostaining (left) and quantification (right) of GFAP (B) and Iba1 (C) in the cerebral cortex and AC3 in cerebellum (D) of WT and *Wdr91* cKO mice at P21. Scale bars, 50  $\mu\text{m}$  in B and C; 20  $\mu\text{m}$  in D. For all quantifications,  $\geq 3$  mice in each genotype were analyzed. Error bars represent SEM. Data were from three independent experiments. \*\*,  $P < 0.01$ ; \*\*\*,  $P < 0.001$ .

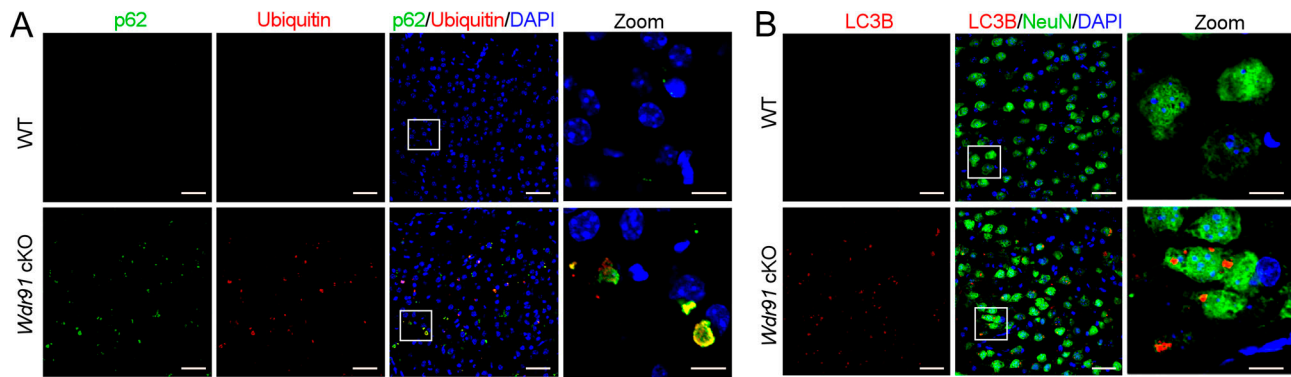


Figure S2. **Loss of WDR91 causes autophagic defects. (A and B)** Coimmunostaining of ubiquitin with p62 (A) and LC3B with NeuN (B) in brain sections of WT and *Wdr91* cKO mice. Nuclei are stained with DAPI (blue). Scale bars, 20  $\mu$ m. Boxed regions are magnified in the rightmost columns (Zoom). Scale bars, 5  $\mu$ m.

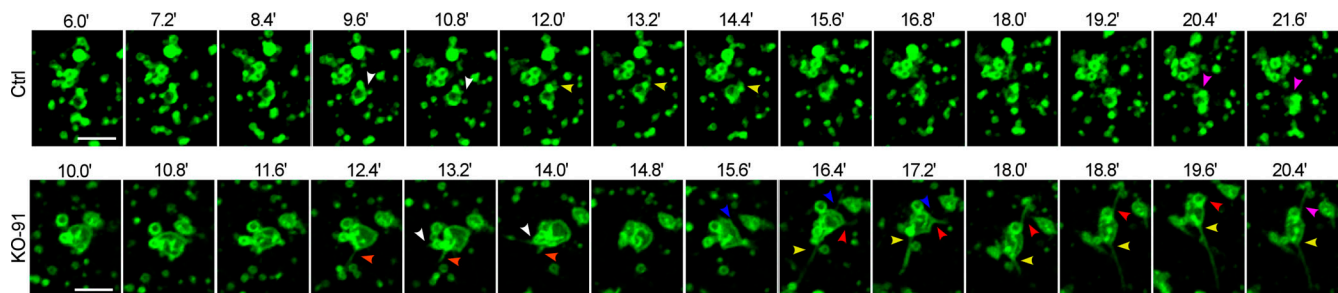


Figure S3. **Time-lapse recording of lysosomal fragmentation and tubulation in LAMP1-GFP-expressing Ctrl and KO-91 HeLa cells treated with AR.** 10 min refers to the time point when AR was added. Colored arrowheads indicate different tubulation events that were followed. Scale bars, 3  $\mu$ m.

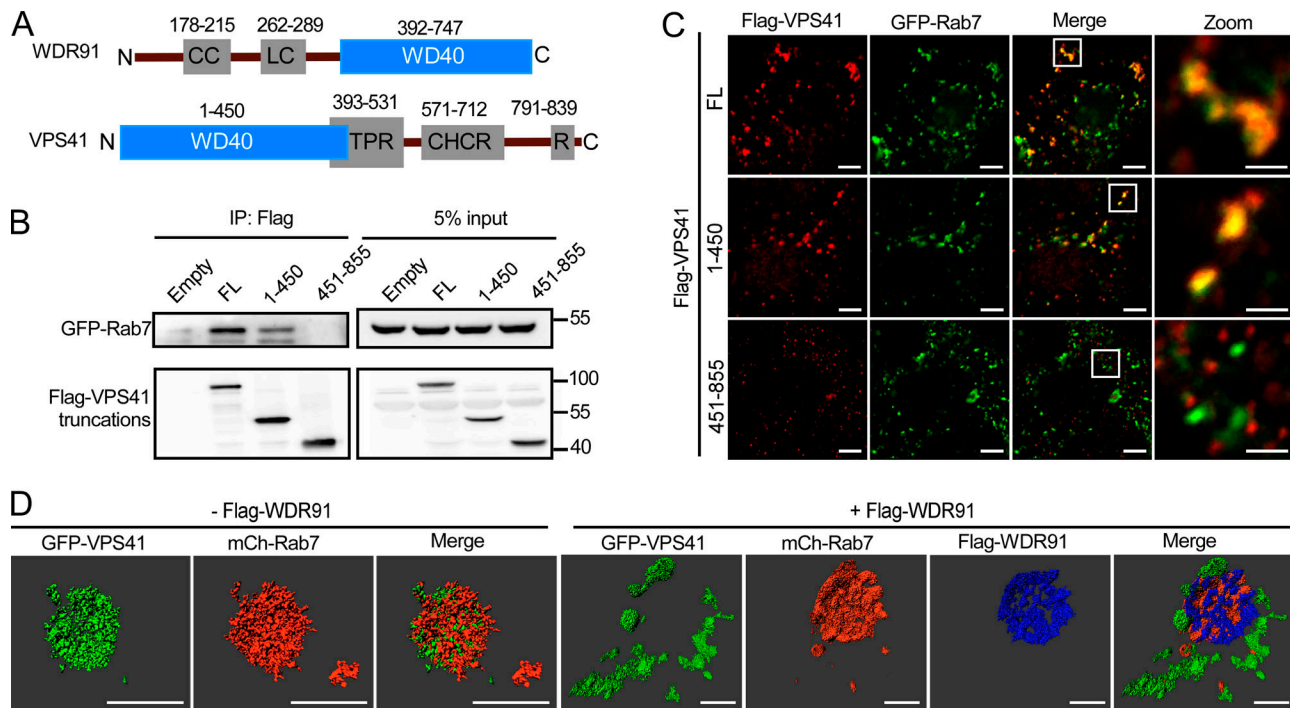


Figure S4. **VPS41 interacts with Rab7 through the WD40 repeats.** **(A)** Schematic representation of the protein domains of WDR91 and VPS41. CC, coiled-coil domain; LC, low complexity; WD40, WD40-repeat containing domain; TPR, tetratricopeptide repeat-like domain; CHCR, clathrin heavy chain repeat; R, RING-H2 zinc finger domain. **(B)** CoIP of GFP-Rab7 with Flag-VPS41 truncations. IP was performed with Flag antibody and detected with antibodies against Flag and GFP. To stabilize the expression of Flag-VPS41<sup>451-855</sup>, cells were treated with MG-132 (0.2  $\mu$ M) for 24 h. **(C)** Colocalization of GFP-Rab7 with Flag-VPS41 truncations in HeLa cells. To stabilize the expression of Flag-VPS41<sup>451-855</sup>, cells were treated with MG-132 (0.2  $\mu$ M) for 24 h. Scale bars, 5  $\mu$ m. Boxed areas are enlarged in the panels labeled Zoom. Scale bars, 2  $\mu$ m. **(D)** 3D reconstruction of the colocalization of GFP-VPS41 and mCh-Rab7 on lysosomes in the absence or presence of Flag-WDR91 in KO-91 HeLa cells, using Imaris software. Scale bars, 2  $\mu$ m.

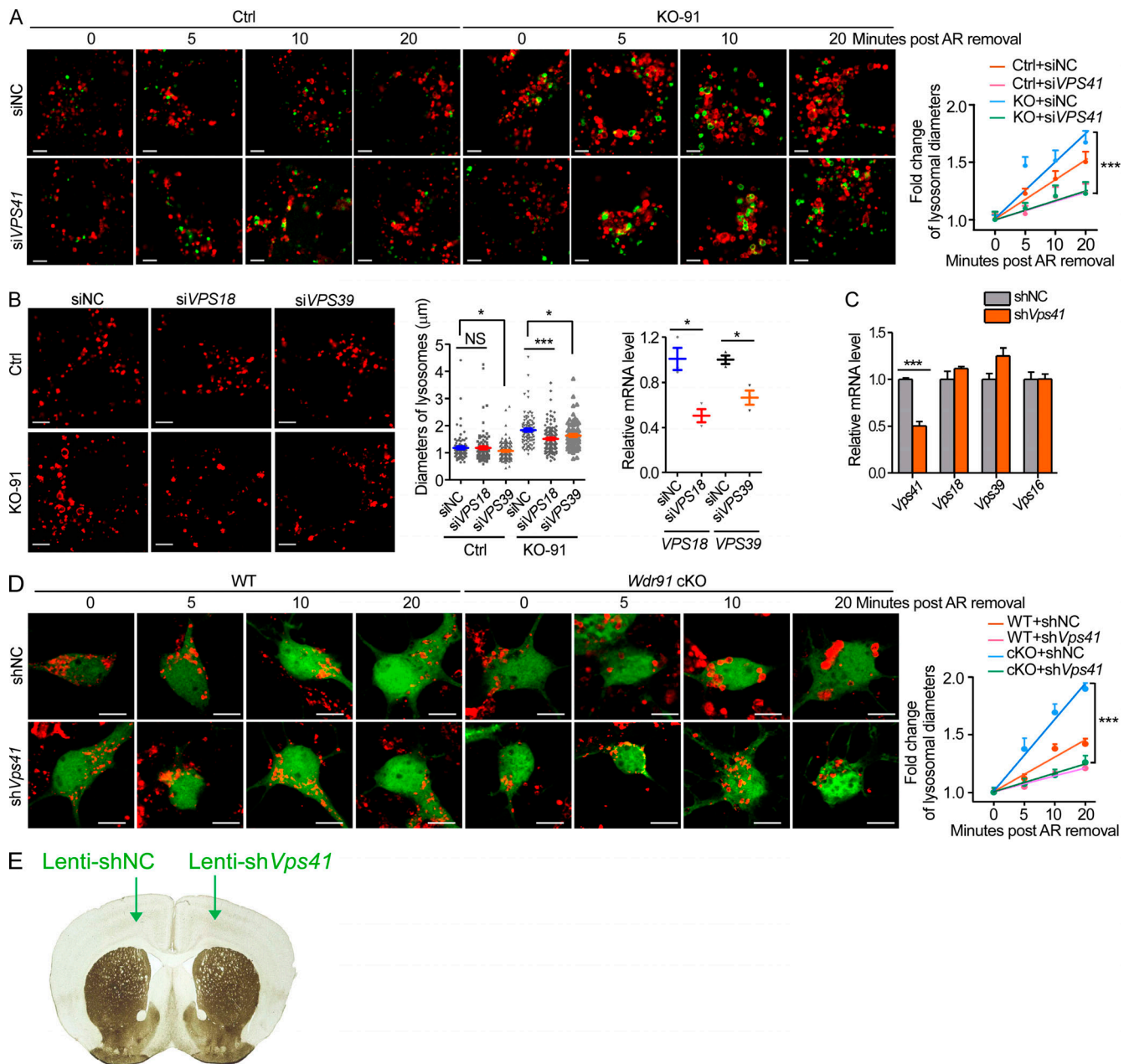


Figure S5. **Inactivation of VPS41 rescues excessive lysosomal fusion caused by WDR91 deficiency.** (A) Immunostaining of LAMP1 (red) and EEA1 (green) in Ctrl or KO-91 HeLa cells expressing negative control siRNA (siNC) or VPS41 siRNA (siVPS41). Cells were treated with AR for 25 min and then returned to normal culture for the indicated time (left). Scale bars, 5  $\mu$ m. Relative change in the size of lysosomes (LAMP1<sup>+</sup>/EEA1<sup>-</sup>) is quantified and shown on the right. (B) Immunostaining of LAMP1 (left) and quantification of lysosome sizes (middle) in Ctrl and KO-91 HeLa cells treated with negative control siRNA (siNC), VPS18 siRNA (siVPS18), or VPS39 siRNA (siVPS39) for 72 h. Scale bars, 5  $\mu$ m. The mRNA levels of VPS18 and VPS39 detected by qPCR in HeLa cells treated with siNC, siVPS18, or siVPS39 are shown on the right. (C) Determining the specificity and efficiency of Vps41 shRNA. N2a cells were transfected with plasmids expressing shVps41, and 72 h after transfection, mRNA levels of indicated genes were examined by qPCR. (D) Left: Immunostaining of LAMP1 (red) in primary neurons expressing negative control shRNA (shNC) or Vps41 shRNA (shVps41). GFP was used as the transfection marker. Neurons were treated with AR for 25 min, and then returned to normal culture for the indicated time (left). Scale bars, 5  $\mu$ m. Relative lysosomal size change is quantified and shown on the right. (E) Schematic diagram of the stereotaxic injection of lentivirus coexpressing GFP and shNC or shVps41. For all quantifications,  $\geq 30$  cells were analyzed for each treatment. Error bars represent SEM. Data were from three independent experiments. \*,  $P < 0.05$ ; \*\*\*,  $P < 0.001$ .

Provided online are three tables. Table S1 lists antibodies and reagents used in the study. Table S2 lists expression vectors used in the study. Table S3 lists oligonucleotides for siRNA and shRNA.